



**HAL**  
open science

# Incorporation and Compensatory Doping Processes of Cu into ZnO Nanowires Investigated at the Local Scale

Manuel Manrique, Bassem Salem, Eirini Sarigiannidou, Hervé Roussel,  
Fabrice Wilhelm, Fabrice Donatini, Véronique Jacob, Gwenaël Le Rhun,  
Vincent Consonni

► **To cite this version:**

Manuel Manrique, Bassem Salem, Eirini Sarigiannidou, Hervé Roussel, Fabrice Wilhelm, et al.. Incorporation and Compensatory Doping Processes of Cu into ZnO Nanowires Investigated at the Local Scale. *Small Structures*, 2024, pp.2400534. 10.1002/sstr.202400534 . hal-04867402

**HAL Id: hal-04867402**

**<https://hal.science/hal-04867402v1>**

Submitted on 8 Jan 2025

**HAL** is a multi-disciplinary open access archive for the deposit and dissemination of scientific research documents, whether they are published or not. The documents may come from teaching and research institutions in France or abroad, or from public or private research centers.

L'archive ouverte pluridisciplinaire **HAL**, est destinée au dépôt et à la diffusion de documents scientifiques de niveau recherche, publiés ou non, émanant des établissements d'enseignement et de recherche français ou étrangers, des laboratoires publics ou privés.



Distributed under a Creative Commons Attribution 4.0 International License

# Incorporation and Compensatory Doping Processes of Cu into ZnO Nanowires Investigated at the Local Scale

Manuel Manrique, Bassem Salem,\* Eirini Sarigiannidou, Hervé Roussel, Fabrice Wilhelm, Fabrice Donatini, Véronique Jacob, Gwenaël Le Rhun, and Vincent Consonni\*

The Cu compensatory doping of ZnO nanowires is of great interest to face the challenge arising from the detrimental screening of the piezoelectric potential generated under mechanical solicitations. However, the incorporation processes of Cu into ZnO nanowires are largely unknown. Here, they are investigated locally by combining mass spectrometry and optical spectroscopy with X-Ray linear dichroism using synchrotron radiation. By varying the  $\text{Cu}(\text{NO}_3)_2/\text{Zn}(\text{NO}_3)_2$  concentration ratio from 0 to 10% in a chemical bath kept at high pH, it is shown that the amount of Cu incorporated into ZnO nanowires varies from around  $4.5 \times 10^{16}$  to  $3.6 \times 10^{18}$  at  $\text{cm}^{-3}$ . However, only 15% of the incorporated Cu forms  $\text{Cu}_{\text{Zn}}$ -related defects, while the remaining Cu lies on the surfaces of ZnO nanowires. Importantly, thermal annealing under  $\text{O}_2$  atmosphere is found to electrically activate the incorporated Cu, resulting in the formation of  $\text{Cu}_{\text{Zn}}$ -related defect complexes involving nearby  $\text{V}_{\text{Zn}}$ , the structured green emission band with a strong phonon coupling, and the increase in the electrical resistivity. These findings shed light on the local environment of Cu incorporated into ZnO nanowires and the required conditions for electrically activating the compensatory doping, as an important outcome for enhanced piezoelectric nanogenerators and stress/strain sensors.

performance of related nanoscale engineering devices.<sup>[1–3]</sup> While ZnO NWs must be highly conductive electrically for optoelectronic and photovoltaic applications,<sup>[1,4]</sup> they are required to be highly resistive electrically for piezoelectric applications.<sup>[5]</sup> In that context, a large number of methods involving vapor phase and wet chemistry deposition techniques have been developed to grow ZnO NWs, offering a wide variety of tunable morphological, optical, and electrical properties.<sup>[6,7]</sup> The chemical bath deposition (CBD), a low-cost technique compatible with green chemistry, is known for its industrial compatibility to fabricate ZnO NW-related devices on both flexible or rigid substrates at low temperatures ranging from 60 to 90 °C.<sup>[8]</sup> Although the morphological properties of ZnO NWs grown by CBD have carefully been optimized, the unintentional incorporation process of H-related defects acting as shallow donors during the growth of ZnO NWs results in a high density of


## 1. Introduction

Zinc Oxide (ZnO), a direct-bandgap compound semiconductor composed of abundant elements, has increasingly received global attention over the past decades, particularly when synthesized in the form of nanowires (NWs) owing to their electronic structure properties that are advantageous to improve the

free electrons,<sup>[9]</sup> typically lying in the range of  $5.0 \times 10^{17}$ – $3.1 \times 10^{19} \text{ cm}^{-3}$ .<sup>[9–11]</sup> These free electrons deteriorate the piezoelectric properties of ZnO NWs through the detrimental screening effect, which refers to the electrostatic interaction between these free carriers and the positive pole created in a mechanically solicited ZnO NW.<sup>[12]</sup> Consequently, a reduction or even a total neutralization of the piezoelectric potential created between the

M. Manrique, E. Sarigiannidou, H. Roussel, V. Consonni  
CNRS, Grenoble INP, LMGP  
Université Grenoble Alpes  
F-38000 Grenoble, France  
E-mail: vincent.consonni@grenoble-inp.fr

M. Manrique, B. Salem  
CNRS, CEA/LETI Minatec, Grenoble INP, LTM  
Université Grenoble Alpes  
38054 Grenoble, France  
E-mail: bassem.salem@cea.fr

 The ORCID identification number(s) for the author(s) of this article can be found under <https://doi.org/10.1002/ssstr.202400534>.

© 2024 The Author(s). Small Structures published by Wiley-VCH GmbH. This is an open access article under the terms of the Creative Commons Attribution License, which permits use, distribution and reproduction in any medium, provided the original work is properly cited.

DOI: 10.1002/ssstr.202400534

M. Manrique, G. Le Rhun  
CEA, LETI  
Université Grenoble Alpes  
F-38000 Grenoble, France

F. Wilhelm  
European Synchrotron Radiation Facility (ESRF)  
71 avenue des Martyrs, 38043 Grenoble, France

F. Donatini  
CNRS, Grenoble INP, Institut NEEL  
Université Grenoble Alpes  
F-38000 Grenoble, France

V. Jacob  
CNRS, IRD, Grenoble INP, IGE  
Université Grenoble Alpes  
F-38000 Grenoble, France

positive and negative poles of the same mechanically solicited ZnO NW proceeds. To overcome the critical issue of screening effect,<sup>[12]</sup> the intentional doping with rare-earth elements<sup>[13]</sup> and the compensatory doping with acceptors<sup>[14,15]</sup> have emerged as two promising solutions. Among the variety of acceptors from I–A, V–A and I–B groups,<sup>[16]</sup> copper (Cu), as an abundant and low-cost element, has been found to be a great candidate due to its similar ionic radius as Zn, which could easily promote the formation of Cu<sub>Zn</sub> with a relatively low ionization energy.<sup>[17,18]</sup> A previous work conducted by Joo et al. presented an original approach to successfully modify the aspect ratio of ZnO NWs using different metallic dopants through adsorption processes assisted by face-selective electrostatic interactions.<sup>[19]</sup> This approach involves the adjustment of the pH-dependent electrostatic interactions between the different metallic species (such as Al, Ga, Cu) and the polar *c*-plane top face and nonpolar *m*-plane sidewalls of ZnO NWs in aqueous solution.<sup>[20–22]</sup> However, the specific incorporation process of the different metallic species acting as dopants into the crystallographic structure of ZnO NWs has poorly been documented so far. Nowadays, the doping of ZnO NWs by CBD with different metallic species, namely as M(X), has largely been investigated and established through the favorable thermodynamic conditions: i) a low supersaturation level in the chemical bath (i.e. supersaturation refers to the difference between the initial concentration of M<sup>X+</sup> ions and the concentration at the thermodynamic equilibrium of soluble M(X) species)<sup>[14,21,23]</sup> and ii) a decrease in the free energy of the adsorption process, which involves the contribution of chemical, electrostatic, and solvation energies.<sup>[24,25]</sup> Using CBD operating in an aqueous solution, those thermodynamic conditions are strongly conducted by the pH adjustment of the chemical bath,<sup>[20]</sup> that is, the pH is the key factor for the nucleation, growth, and doping processes of ZnO NWs. Lausecker et al. showed that when Zn(II) and Cu(II) species are simultaneously present in the chemical bath, three main pH regions are classified according to the supersaturation level at 85 °C:<sup>[22]</sup> i) the low-pH environment between 5.2 and 5.7, where shorter heterogeneously formed ZnO NWs are synthesized along with a low precipitation of Cu-related solid phases; then, ii) the intermediate-pH environment from 5.7 to 8.0, where the highest supersaturation level results in a massive precipitation of ZnO<sub>(s)</sub> and Cu-related solid phases that avoid the heterogeneous growth of ZnO NWs; and finally iii) the high-pH region between 8.0 and 8.7, where longer heterogeneously formed ZnO NWs are grown and the precipitation of Cu-related solid phases is thermodynamically not favorable. Therefore, it has been well established that the Cu doping of ZnO NWs should be performed in a chemical bath maintained in a high-pH environment. The adsorption process of Cu dopants can further be assisted by electrostatic forces between the positively charged Cu(II) species and negatively charged faces of ZnO NWs.<sup>[22]</sup> Under these oxygen-rich conditions, the Cu dopants are also expected to substitute for Zn sites as Cu<sub>Zn</sub> acceptors with a low formation energy, according to density functional theory calculations.<sup>[26]</sup> Interestingly, the Cu doping was recently found to successfully enhance the piezoelectric properties of ZnO NWs when integrated into a piezoelectric nanogenerator (PNG) in the vertically integrated configuration.<sup>[15]</sup> A fixed concentration of Cu dopants resulted in an increase in the electrical resistivity of ZnO NWs grown by

CBD, reducing the density of free electrons through electron–hole pair recombination processes. This led to the decrease in the magnitude of the screening effect within the mechanically solicited ZnO NWs, in turn enhancing the output voltage of the PNG. Despite the resulting great interest for piezoelectric applications, the effects of different Cu doping levels on the structural, physicochemical, optical, and electrical properties of ZnO NWs remain still unclear, along with a careful investigation of the local environment around Cu dopants.

In this study, ZnO NWs are synthesized by CBD with [Cu(NO<sub>3</sub>)<sub>2</sub>]/[Zn(NO<sub>3</sub>)<sub>2</sub>] ratios of 0, 1, 3, 5, and 10% in the chemical bath. The adsorption and incorporation processes of Cu dopants in ZnO NWs are studied in detail before and after thermal annealing under O<sub>2</sub> atmosphere by coupling thermodynamic computations, in situ pH measurements, and inductively coupled plasma mass spectrometry (ICP-MS). The resulting morphological and structural properties are assessed by field-emission scanning electron microscopy (FESEM), X-Ray diffraction (XRD), and Raman scattering. The incorporation of Cu dopants into ZnO NWs and the local environment around them are further investigated by 5 K cathodoluminescence, X-Ray absorption near-edge structure (XANES), and X-Ray linear dichroism (XLD). The effect of the Cu compensatory doping on the electrical properties of ZnO NWs is eventually revealed through two-point probe electrical resistivity measurements. A comprehensive overview of the doping processes with Cu is further gained as an invaluable mean to optimize the performance of piezoelectric devices made of Cu-doped ZnO NWs.

## 2. Results

### 2.1. Morphological and Physicochemical Properties of Cu-Doped ZnO Nanowires

#### 2.1.1. Structural Morphology of Cu-Doped ZnO Nanowires

The homoepitaxial and heterogeneous growth of unintentionally *n*- and Cu-doped ZnO NWs was achieved by CBD on polycrystalline ZnO seed layers oriented along the polar *c*-axis.<sup>[27]</sup> The morphological properties of ZnO NWs with a [Cu(NO<sub>3</sub>)<sub>2</sub>]/[Zn(NO<sub>3</sub>)<sub>2</sub>] ratio in the chemical bath (denoted as [Cu]/[Zn]<sub>bath</sub>) varying in the range of 0–10% are presented in **Figure 1a–e**. The resulting mean diameter measured at half of the height of the pristine ZnO NWs, their mean length, their aspect ratio defined as the ratio of their mean length over their mean diameter, as well as their number density are summarized in **Figure 1f**. The ZnO NWs are vertically aligned and exhibit a pencil-shaped top face, due to the axial growth rate along the polar *c*-axis that is higher than the radial growth rate along the nonpolar *m*-axis. Through the gradual increase in the [Cu]/[Zn]<sub>bath</sub> ratio, a progressive increase in the mean diameter of ZnO NWs from about 105 to 142 nm occurs, along with a progressive decrease in their mean length from about 7.9 to 5.6 μm. Hence, the aspect ratio of ZnO NWs is found to decrease from about 75 to 39 as the [Cu]/[Zn]<sub>bath</sub> ratio is increased from 0 to 10%. The number density of ZnO NWs lies in the range of 30–40 NW μm<sup>−2</sup> and does not show any particular tendency as a function of [Cu]/[Zn]<sub>bath</sub> ratio. The present finding is

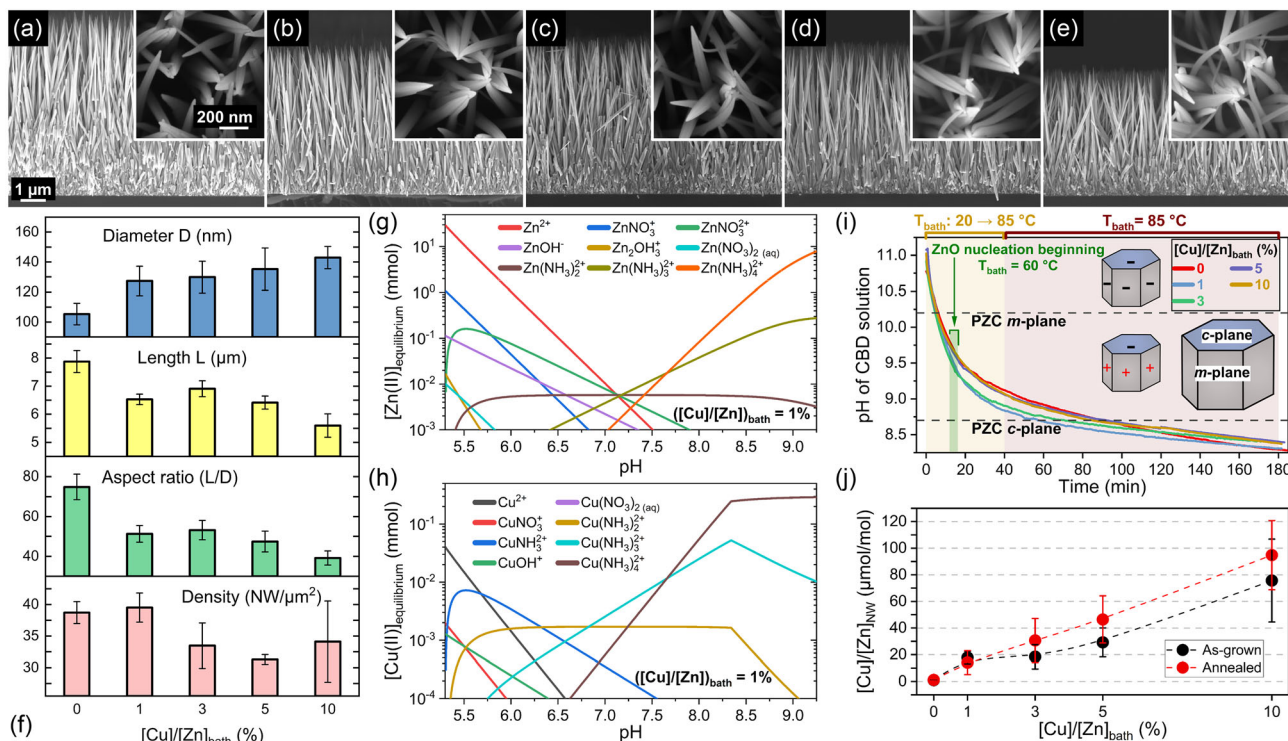


**Figure 1.** Cross-sectional and top-view (inset) FESEM images of ZnO NWs grown by CBD at 85 °C for 3 h with  $[Cu]/[Zn]_{bath}$  ratios of a) 0, b) 1, c) 3, d) 5, and e) 10%, respectively. f) Resulting mean diameter, mean length, aspect ratio, and number density of ZnO NWs grown by CBD at different  $[Cu]/[Zn]_{bath}$  ratios. Theoretical solubility plots of g) Zn(II) and h) Cu(II) species at 85 °C according to Visual MINTEQ software, using the initial concentrations of  $Zn^{2+}$  and  $Cu^{2+}$  ions corresponding to 30 and 0.3  $mmol L^{-1}$ , respectively. i) In situ pH measurements of the chemical bath during the growth of ZnO NWs at different  $[Cu]/[Zn]_{bath}$  ratios. The insets represent the expected surface electrical charge of the different crystallographic planes of ZnO NWs according to the PZC values reported in Refs. [32,33,87]. j) Atomic  $[Cu]/[Zn]_{NW}$  ratio inferred from ICP-MS of ZnO NWs grown by CBD at different  $[Cu]/[Zn]_{bath}$  ratios. The annealed series corresponds to ZnO NWs thermally annealed at 500 °C for 1 h under  $O_2$  atmosphere.

consistent with the fact that the number density of unintentionally *n*- and Cu-doped ZnO NWs is governed by the number of nucleation sites on the polycrystalline ZnO seed layers.<sup>[28]</sup> In addition, no morphological changes of the pristine ZnO NWs regarding their shape and dimensions proceed after thermal annealing at 500 °C for 1 h under  $O_2$  atmosphere, as shown in Figure S1, Supporting Information.

### 2.1.2. Physicochemical Adsorption Process of Cu(II)-Related Species

To understand the physicochemical and adsorption processes of the Zn(II) and Cu(II) species occurring throughout the growth of ZnO NWs by CBD, the corresponding speciation diagrams are respectively plotted in Figure 1g,h using Visual MINTEQ software. A  $[Cu]/[Zn]_{bath}$  ratio of 1% was considered for the thermodynamic computations, by fixing the initial concentration of  $Zn^{2+}$  and  $Cu^{2+}$  ions at 30 and 0.3  $mmol L^{-1}$ , respectively. The pH was further set by varying the concentration of  $NH_4^+$  ions from 0 to 2500  $mmol L^{-1}$  at 85 °C. At the thermodynamic equilibrium reached at 85 °C, the main Zn(II) species in the chemical bath are  $Zn^{2+}$  ions and  $Zn(NH_3)_4^{2+}$  complexes in the pH regions below  $\approx 7$  (low-pH environment) and above  $\approx 7.7$  (high-pH

environment), respectively. Interestingly, a similar behavior is revealed for Cu(II) species, which form  $Cu^{2+}$  ions and  $Cu(NH_3)_4^{2+}$  complexes in the low-pH and high-pH environments, respectively. The characteristics of the speciation diagrams along with the similar ionic radii of Zn(II) and Cu(II) ions strongly suggest the occurrence of identical adsorption processes during the growth of ZnO NWs by CBD.<sup>[17]</sup> It is worth mentioning that the speciation diagrams of the Zn(II) and Cu(II) species for the  $[Cu]/[Zn]_{bath}$  ratios of 1, 3, 5, and 10% reveal the same formation of Zn- and Cu-related species as a function of pH. The nature of the predominant Zn- and Cu-related species as a function of pH thus does not depend on the  $[Cu]/[Zn]_{bath}$  ratio lying in the range of 1–10%. The only difference among the present speciation diagrams is related to the supersaturation levels of Cu(II) and Zn(II) species. Indeed, by adding a higher concentration of  $Cu(NO_3)_2$  in the chemical bath, the supersaturation level of Cu(II) species slightly increases, while the supersaturation level of Zn(II) species decreases. Therefore, a competitive adsorption process between the Zn(II) and Cu(II) species and thus a competitive incorporation process of Zn and Cu atoms occurs throughout the growth of ZnO NWs. This affects the morphology of ZnO NWs, which switches from larger to shorter NWs as the  $[Cu]/[Zn]_{bath}$  ratio



is increased as summarized in Figure 1f. Moreover, the addition of a higher concentration of  $\text{Cu}(\text{NO}_3)_2$  in the chemical bath also influences the nucleation process of ZnO NWs,<sup>[29]</sup> which has been reported using hexamethylenetetramine (HMTA) and polyethylenimine (PEI) molecules.<sup>[28,30]</sup> According to the X-Ray pole figures of ZnO NWs shown in Figure S2, Supporting Information, the (002), (101), and (112) ZnO diffraction peaks show a progressive tilting increase from 9.1 to 13.3° with the increase in the  $[\text{Cu}]/[\text{Zn}]_{\text{bath}}$  ratio from 0 to 10%. This suggests a direct competition of Zn(II) and Cu(II) species at the very beginning of the nucleation step of the ZnO NWs, occurring on the semipolar and polar *c*-planes of ZnO grains in the polycrystalline seed layer.<sup>[31]</sup> Subsequently, it should be noted that the polar *c*-plane top facet and nonpolar *m*-plane sidewalls of ZnO NWs are positively or negatively charged, owing to the formation of  $-\text{OH}_2^+$  and  $-\text{O}^-$  groups at the surfaces, respectively.<sup>[20]</sup> The electrical transition from positively to negatively charged surfaces occurs for a given pH value called the point-of-zero-charge (PZC), located at  $8.7 \pm 0.2$  and  $10.2 \pm 0.2$  for the polar *c*-plane and non-polar *m*-planes of ZnO NWs, respectively.<sup>[32,33]</sup>

The in situ pH measurements confirm the growth of ZnO NWs by CBD in the high-pH environment after thermalization of the chemical bath at 85 °C, as shown in Figure 1i, in which the  $\text{Zn}(\text{NH}_3)_4^{2+}$  and  $\text{Cu}(\text{NH}_3)_4^{2+}$  complexes are the main expected Zn(II) and Cu(II) species, respectively. Therefore, the electrostatic forces between the positively charged  $\text{Cu}(\text{NH}_3)_4^{2+}$  complexes and the negatively charged polar *c*-planes of ZnO NWs assist the adsorption process of Cu(II) species. The Coulomb interactions lead to favorable changes in the electrostatic free energy. The latter combined with the chemical free energy (involving surface hydrogen bonding and short-range dispersion forces) results in a cumulative energy that overcomes the solvation free energy barrier (defined as the solvation energy change of an ion moving from the bulk to the interfacial region). This results in the establishment of advantageous thermodynamic conditions for the adsorption process of Cu(II) species on the outside Stern plane of solid ZnO NW faces.<sup>[22,24,25]</sup> Consequently, a progressive increase in the amount of Cu(II) species adsorbed on the surfaces of ZnO NWs, and thus of Cu incorporated onto the surfaces of ZnO NWs and into their bulk, denoted as  $[\text{Cu}]/[\text{Zn}]_{\text{NW}}$ , is expected as the  $[\text{Cu}]/[\text{Zn}]_{\text{bath}}$  ratio is increased. This is successfully shown using ICP-MS measurements, as presented in Figure 1j, where the atomic  $[\text{Cu}]/[\text{Zn}]_{\text{NW}}$  ratio increases from 2 to  $80 \mu\text{mol mol}^{-1}$  as the  $[\text{Cu}]/[\text{Zn}]_{\text{bath}}$  ratio is increased from 0 to 10%. Interestingly, the atomic  $[\text{Cu}]/[\text{Zn}]_{\text{NW}}$  ratios roughly keep the same values after thermal annealing at 500 °C for 1 h under  $\text{O}_2$  atmosphere. Accordingly, considering six atoms of Zn in one crystallographic unit cell (i.e.,  $4.2 \times 10^{22}$  at  $\text{cm}^{-3}$  of Zn), the amount of Cu is around  $4.50 \pm 0.50 \times 10^{16}$ ,  $6.71 \pm 1.11 \times 10^{17}$ ,  $1.03 \pm 0.36 \times 10^{18}$ ,  $1.59 \pm 0.51 \times 10^{18}$ , and  $3.58 \pm 0.56 \times 10^{18}$  at  $\text{cm}^{-3}$  in ZnO NWs grown by CBD before and after thermal annealing for the given  $[\text{Cu}]/[\text{Zn}]_{\text{bath}}$  ratio of 0, 1, 3, 5, and 10%, respectively. It is worth mentioning that the lowest amount of Cu in ZnO NWs when grown with the  $[\text{Cu}]/[\text{Zn}]_{\text{bath}}$  ratio of 0%, that is, no Cu dopant solution added in the chemical bath, is due to the significant amount of Cu residual impurities in the chemical precursors used as zinc nitrate, HMTA, and ammonia. In addition, the

quantification of Cu by ICP-MS involves the Cu dopants located both on the surfaces of ZnO NWs and in their bulk.

## 2.2. Raman Spectroscopy of As-Grown and Thermally Annealed Cu-Doped ZnO Nanowires

The Raman scattering spectra of as-grown and thermally annealed ZnO NWs with a  $[\text{Cu}]/[\text{Zn}]_{\text{bath}}$  ratio varying in the range of 0–10% were recorded in the low- and high-wavenumber regions, as presented in Figure 2a,b, respectively. All the Raman scattering spectra were normalized and calibrated according to the intensity and position of the Si Raman line at  $520.7 \text{ cm}^{-1}$ , respectively. In the low-wavenumber region of  $80\text{--}920 \text{ cm}^{-1}$ , the typical phonon modes assigned to the wurtzite structure of ZnO NWs occur: the main Raman lines are located at 99 ( $E_2^{\text{low}}$ ), 380 ( $A_1(\text{TO})$ ), 434 ( $E_2^{\text{high}}$ ), and 581 ( $A_1(\text{LO})$ )  $\text{cm}^{-1}$ , along with the second-order Raman lines at 204 ( $2\text{TA}/2 E_2^{\text{low}}$ ) and 333 ( $E_2^{\text{high}} - E_2^{\text{low}}$ )  $\text{cm}^{-1}$ . In the high-wavenumber region of  $2600\text{--}3750 \text{ cm}^{-1}$ , the Raman lines attributed to carbon-, nitrogen-, and hydrogen-related defects occur. The broad Raman band lying from  $2850$  to  $2990 \text{ cm}^{-1}$  is assigned to phonon modes induced by the symmetric and antisymmetric stretching bonds of  $\text{C-H}_x$  ( $x = 1, 2, 3$ ),<sup>[34]</sup> as a result of an adsorption process of carbon on the *m*-plane sidewalls of ZnO NWs coming from the HMTA molecules.<sup>[28]</sup> Then, a weak Raman line is detected at  $3073 \text{ cm}^{-1}$  and related to  $\text{V}_{\text{Zn}}\text{-N}_\text{O}\text{-H}$  complexes,<sup>[35]</sup> followed by the occurrence of  $\text{N}_\text{O}\text{-H}$ -related phonons in the wavenumber region of  $3100\text{--}3200 \text{ cm}^{-1}$ .<sup>[36,37]</sup> Moreover, the  $\text{V}_{\text{Zn}}\text{-nH}$  ( $n = 1, 2, 3$ ) defect complexes lead to the broad Raman band observed from  $3300$  to  $3450 \text{ cm}^{-1}$ .<sup>[38–40]</sup> The asymmetric Raman shoulder lying between  $3300$  and  $3650 \text{ cm}^{-1}$  involves the contribution of  $\text{O-H}$  bonds<sup>[41]</sup> on the surfaces of ZnO NWs and of  $\text{H}_{\text{BC}}$ <sup>[42]</sup> in their bulk.

By performing the thermal annealing of ZnO NWs at 500 °C for 1 h under  $\text{O}_2$  atmosphere, several significant changes in the Raman scattering spectra arise, including the appearance of additional modes (AMs) in the low-wavenumber region and the apparent vanishing of Raman lines in the high-wavenumber region. Regardless of the  $[\text{Cu}]/[\text{Zn}]_{\text{bath}}$  ratio of 0–10%, the occurrence of typical AMs after thermal annealing of ZnO NWs is depicted in the low-wavenumber region at 276 ( $B_1^{\text{low}}$ ), 581 ( $B_1^{\text{high}}$ ), 644 ( $\text{TA} + B_1^{\text{high}}$ ), 668 ( $\text{TA} + \text{LO}$ ), and 856 ( $B_1^{\text{low}} + B_1^{\text{high}}$ )  $\text{cm}^{-1}$ .<sup>[43,44]</sup> These AMs are mainly due to the presence of silent Raman modes related to Al, Ga, Sb, and Fe as extrinsic impurities in ZnO NWs following the addition of ammonia in the chemical bath,<sup>[43]</sup> whose the activation proceeds through the breakdown of the translational crystal symmetry upon thermal annealing.<sup>[45]</sup> A massive migration process of hydrogen in the form of  $\text{H}_{\text{BC}}$  further occurs towards the surfaces of ZnO NWs upon thermal annealing, where they recombine to form  $\text{H}_2$  molecules leading to the vanishing of the different Raman lines attributed to hydrogen-related defects in the high-wavenumber region.<sup>[34,35]</sup>

Moreover, no Raman lines related to any  $\text{Cu}_2\text{O}$ ,  $\text{CuO}$ , or  $\text{Cu}(\text{OH})_2$  phases are detected.<sup>[46]</sup> This is in agreement with the XRD patterns as presented in Figure S3, Supporting Information, where no diffraction peaks related to any  $\text{Cu}_2\text{O}$ ,  $\text{CuO}$ , or  $\text{Cu}(\text{OH})_2$  phases are neither observed. Therefore, no Cu-related solid phases precipitate in the chemical bath in the

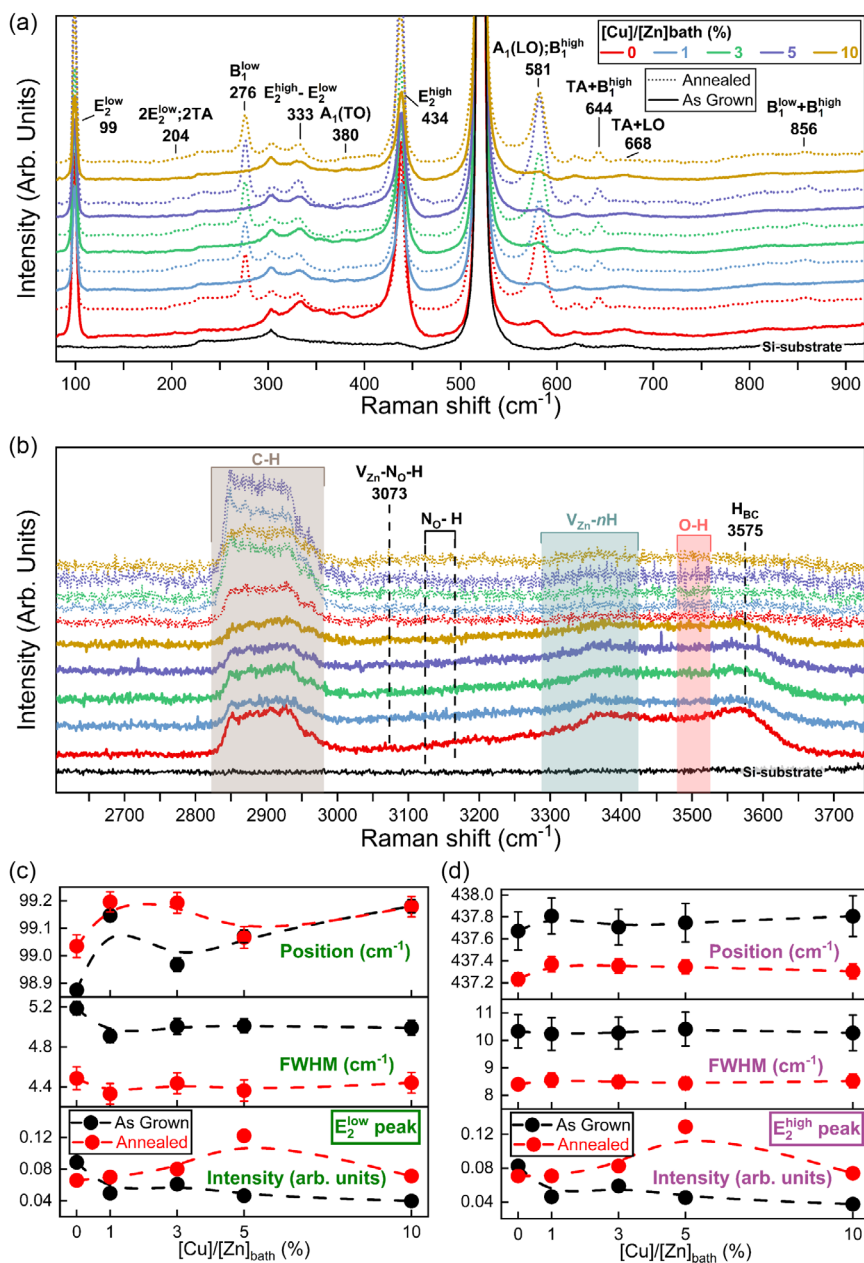


**Figure 2.** Raman scattering spectra of ZnO NWs grown by CBD at 85 °C for 3 h for different  $[Cu]/[Zn]_{bath}$  ratios, before and after thermal annealing at 500 °C for 1 h under  $O_2$  atmosphere, recorded in the a) low- and b) high-wavenumber regions. Evolution of the corresponding characteristics of the c)  $E_2^{low}$  and d)  $E_2^{high}$  Raman lines.

high-pH environment, owing to the unfavorable thermodynamic conditions as suggested by the theoretical solubility plots of Cu(II) species in Figure 1h. It is worth mentioning that the crystallographic properties of ZnO NWs can be correlated with their Raman line features. By focusing on the two intense and narrow  $E_2^{low}$  and  $E_2^{high}$  Raman lines of ZnO NWs, an increase in their intensity as well as a significant reduction of their FWHM occurs after thermal annealing, regardless of the  $[Cu]/[Zn]_{bath}$  ratio of 0–10%, as shown Figure 2c,d. This reveals a strong improvement in the crystallinity of unintentionally *n*- and Cu-doped ZnO NWs after thermal annealing. In addition, the noticeable shift of both

the  $E_2^{low}$  and  $E_2^{high}$  Raman lines towards higher wavenumbers before thermal annealing, as the  $[Cu]/[Zn]_{bath}$  ratio is increased from 0 to 10%, may indicate the generation of a small compressive stress state along the polar *c*-axis within the ZnO NWs. This would be in agreement with the nearly negligible decrease in the lattice parameters *a* and *c*, as reported in Figure S3, Supporting Information. After thermal annealing, the  $E_2^{high}$  Raman line significantly shifts to lower wavenumbers, indicating the relaxation of the compressive stress state and the presence of a residual stress state along the polar *c*-axis due to the reduction of the lattice parameter *a*.<sup>[47]</sup> Correlatively, an opposite shift of the  $E_2^{low}$

Raman line to higher wavenumbers occurs owing to its negative Grüneisen parameter under hydrostatic pressure, as reported in Ref. [48], further confirming the presence of a residual stress state along the polar  $c$ -axis. Moreover, the apparent lattice distortion of ZnO NWs when doped with Cu and after thermal annealing can induce structural potential fluctuations and finite-size effects, resulting in a change of the phonon contribution and subsequently in a modification of the shapes of the  $E_2^{\text{low}}$  and  $E_2^{\text{high}}$  Raman lines.<sup>[49]</sup> Therefore, the unveiled changes in the shapes of the Raman lines along with the slight lattice parameter modification of ZnO NWs suggest the progressive incorporation process of Cu atoms as  $\text{Cu}_{\text{Zn}}$  when the  $[\text{Cu}]/[\text{Zn}]_{\text{bath}}$  ratio is increased. In addition, the absence of any AMs related to the Cu doping of ZnO NWs is consistent with the literature and does not imply the absence of Cu in the crystallographic structure of ZnO NWs.

### 2.3. Optical Spectroscopy of As-Grown and Thermally Annealed Cu-Doped ZnO Nanowires

#### 2.3.1. Cathodoluminescence Spectroscopy of As-Grown Cu-Doped ZnO Nanowires

The 5 K cathodoluminescence spectra of as-grown ZnO NWs with a  $[\text{Cu}]/[\text{Zn}]_{\text{bath}}$  ratio varying in the range of 0–10% are

presented in **Figure 3a**. The near-band-edge (NBE) emission of as-grown ZnO NWs, as shown in the inset of Figure 3a, is centered at  $\approx 3.342$  eV when the  $[\text{Cu}]/[\text{Zn}]_{\text{bath}}$  ratio is of 0%, and relatively broad with a FWHM of 133 meV. It is composed of the main H-related donor-bound exciton ( $\text{D}^\circ\text{X}$ ) lines<sup>[9]</sup> at 3.3601 ( $\text{H}_{\text{BC}}$ ),<sup>[50]</sup> 3.3614 ( $\text{V}_{\text{Zn}}\text{-3H}$ ,  $\text{I}_5$  line),<sup>[51]</sup> and 3.3628 ( $\text{H}_{\text{O}}$ ,  $\text{I}_4$  line) eV,<sup>[50,52]</sup> as well as the associated two-electron satellite (TES) lines in the range of 3.316–3.333 eV. In addition, radiative transitions involving extended defects resulting from the coalescence of grains in polycrystalline ZnO seed layers are also expected.<sup>[53]</sup> The visible emission band is in contrast centered at  $\approx 2.0$  eV and intense, as shown in Figure 3a. It involves the emissions resulting from transition levels ( $\epsilon$ ) attributed to  $\text{V}_{\text{Zn}}$ -related defect complexes.<sup>[9,35]</sup> The red–orange emission band (1.6–2 eV) originates from deep acceptors such as  $[\text{V}_{\text{Zn}}\text{-H}]^{\epsilon(0/-1)}$  and  $[\text{V}_{\text{Zn}}\text{-N}_{\text{O}}\text{-H}]^{\epsilon(0/-1)}$  defect complexes, which share an emission energy of 1.82 eV, as well as  $[\text{V}_{\text{Zn}}]^{\epsilon(-1/-2)}$  defects with an emission energy of 1.6 eV.<sup>[9,35]</sup> The yellow emission band (2–2.3 eV) results from  $[\text{V}_{\text{Zn}}\text{-2H}]^{\epsilon(+1/0)}$  and  $[\text{V}_{\text{Zn}}\text{-N}_{\text{O}}\text{-H}]^{\epsilon(0/-1)}$  defect complexes with an emission energy of 2.29 and 2.27 eV, respectively.<sup>[9,35]</sup> The green emission band (2.3–2.5 eV) is instead assigned to surface-related effects.<sup>[9,54]</sup> Interestingly, as the  $[\text{Cu}]/[\text{Zn}]_{\text{bath}}$  ratio is increased from 0% to 10%, the intensity of the corresponding NBE emission is drastically reduced and

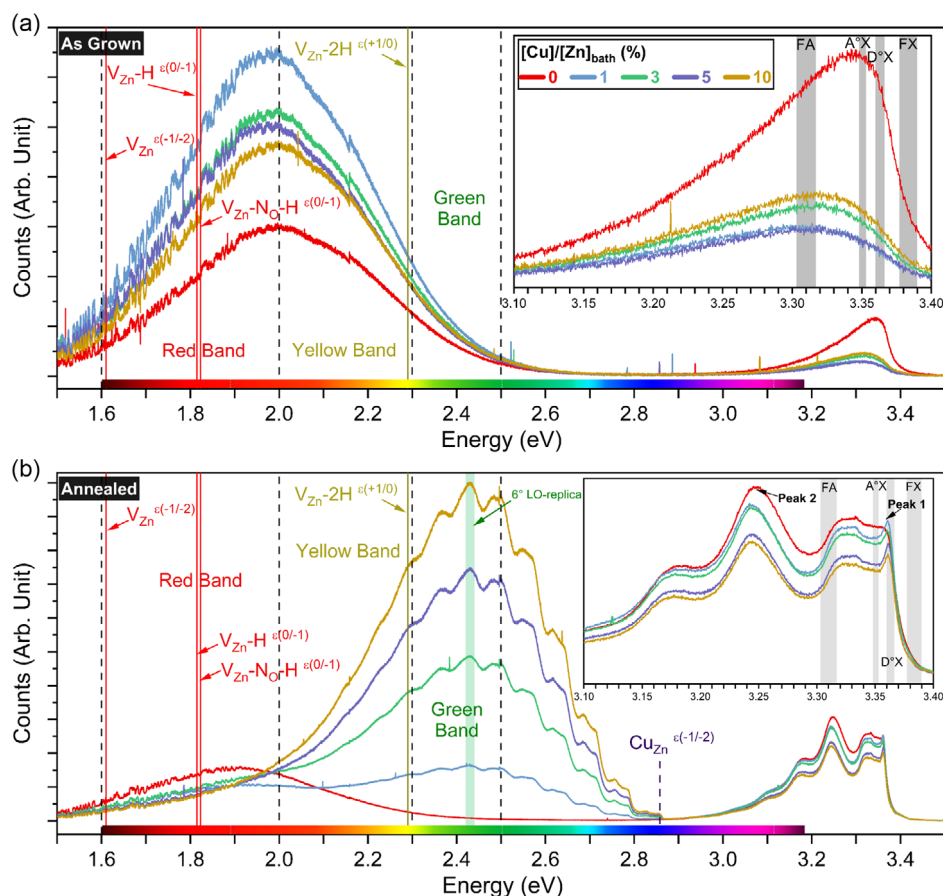


**Figure 3.** 5 K cathodoluminescence spectra of ZnO NWs grown by CBD with  $[\text{Cu}]/[\text{Zn}]_{\text{bath}}$  ratios of 0, 1, 3, 5, and 10%, a) before and b) after thermal annealing at 500 °C for 1 h under  $\text{O}_2$  atmosphere, along with their respective NBE emissions as insets.

centered at  $\approx 3.311$  eV, resulting in a redshift of about 31 meV, while its FWHM increases to 160 meV. Concomitantly, the intensity of the visible emission band is significantly increased, which may be related to the change of the concentration of  $V_{Zn}$ -related defect complexes<sup>[9]</sup> both in the bulk and on the surfaces of as-grown Cu-doped ZnO NWs.

### 2.3.2. Cathodoluminescence Spectroscopy of Thermally Annealed Cu-Doped ZnO Nanowires

The 5 K cathodoluminescence spectra of thermally annealed ZnO NWs with a  $[Cu]/[Zn]_{bath}$  ratio varying in the range of 0–10% are presented in Figure 3b. Following thermal annealing of unintentionally *n*- and Cu-doped ZnO NWs at 500 °C for 1 h under  $O_2$  atmosphere, a noteworthy change of their cathodoluminescence spectra is depicted in Figure 3b. The NBE emission of thermally annealed ZnO NWs, as shown in the inset of Figure 3b, reveals a sharp line located at  $\approx 3.362$  eV (denoted as Peak-1) within the region where the  $H_O$  ( $I_4$  line) contribution is expected,<sup>[50,52]</sup> specifically as the  $[Cu]/[Zn]_{bath}$  ratio is above 0%. In this same region, the  $D^*X$  lines from Al- and Ga-related extrinsic donors occur at 3.3606 ( $Al_{Zn}$ ,  $I_6$  line) and 3.3598 ( $Ga_{Zn}$ ,  $I_8$  line) eV,<sup>[51,55]</sup> which is in agreement with their corresponding AMs observed in the Raman scattering spectra after thermal annealing. As a result, it is expected that the slight lattice distortion originating from the incorporation process of Cu dopants as  $Cu_{Zn}$  likely favors the formation of  $Al_{Zn}$  and  $Ga_{Zn}$  extrinsic donors and hence the development of Peak-1. Accordingly, the intensity of Peak-1 steadily decreases as the  $[Cu]/[Zn]_{bath}$  ratio is increased from 0 to 10%, resulting from a competitive process with the predominant formation of  $Cu_{Zn}$  defects with respect to  $Al_{Zn}$  and  $Ga_{Zn}$  extrinsic donors. Then, the broad shoulder centered at  $\approx 3.325$  eV is assigned to the associated TES lines.<sup>[50]</sup> In contrast, the prominent line located at  $\approx 3.247$  eV (denoted as Peak-2) dominates the NBE emission, with its first and second longitudinal optical (LO) phonon replica at 3.171 and 3.097 eV, respectively. Peak-2 is mainly associated with donor-acceptor pair (DAP) transitions related to a compensatory process of donor-acceptor pairs involving  $V_{Zn}$ ,  $V_{Zn}-H$ , and  $V_{Zn}-N_O-H$  defect complexes acting as deep acceptors.<sup>[44,56]</sup> The slight redshift of Peak-2 as the  $[Cu]/[Zn]_{bath}$  ratio is increased from 0 to 10% suggests a progressive increase in the concentration of acceptor defects contributing to DAP transitions. Importantly, the visible emission band of unintentionally *n*- and Cu-doped ZnO NWs is the most affected one following thermal annealing, as presented in Figure 3b. Unintentionally *n*-doped ZnO NWs show a redshift from 2 to  $\approx 1.9$  eV of the red-orange emission band after thermal annealing, which is in agreement with the expected massive formation of  $V_{Zn}$ -related defect complexes acting as deep acceptors.<sup>[44,56]</sup> Very interestingly, as the  $[Cu]/[Zn]_{bath}$  ratio is increased from 1 to 10%, the visible band emission is strongly altered with a prominent peak at 2.428 eV corresponding to the 6°-LO phonon replica of the zero-phonon line (ZPL) located at  $E_{ZPL} \approx 2.856$  eV and involving  $[Cu_{Zn}^{2+}]^{e(-1/-2)}$  acceptor defects.<sup>[57,58]</sup> The complete sets of LO phonon replica of the ZPL are separated by  $\approx 70$  meV and are located at 2.785, 2.711, 2.642, 2.570, 2.495, 2.428, 2.362, 2.293, and 2.226 eV corresponding to the (1°–9°) LO phonon replica, respectively. The strong phonon

coupling was assessed through the determination of the Huang–Rhys constant *S*, for which the values were found to be  $(6.61 \pm 0.11)$ ,  $(6.45 \pm 0.08)$ ,  $(6.40 \pm 0.07)$ , and  $(6.36 \pm 0.06)$  in the case of ZnO NWs grown with  $[Cu]/[Zn]_{bath}$  ratios of 1, 3, 5, and 10%, respectively.

### 2.3.3. Optical Signature of Cu Dopants into ZnO Nanowires

The ZPL emission peak is assigned to the radiative transitions from a  $(Cu^+, h)$  short excited state to the  $Cu^{2+}$  ( $^2T_2$ ) ground state.<sup>[59]</sup> When a neighboring O atom transfers one electron to the neutral acceptor  $Cu^{2+}$ , the negatively charged acceptor  $Cu^{1+}$  is created, which undergoes a transition to the  $(Cu^+, h)$  excited state by capturing the free hole from a created free exciton under electron beam illumination. The  $(Cu^+, h)$  excited state, located at  $\approx 0.4$  eV above the valence band maximum, thus leads to the emission of a photon when the free hole is captured by the potential created by the tenth electron of the *d*-orbital of  $Cu^+$ , resulting in the  $Cu^{2+}$  ( $^2T_2$ ) ground state located at  $\approx 0.2$  eV below the conduction band minimum.<sup>[59,60]</sup> Therefore, the greatly enhanced green emission band as the  $[Cu]/[Zn]_{bath}$  ratio is increased from 1 to 10% and following thermal annealing likely involves: 1) the surface-to-bulk migration process of  $Cu_{Zn}$  acceptors defects through the massive creation of  $V_{Zn}$  defects in ZnO NWs under  $O_2$  atmosphere<sup>[61]</sup> as well as 2) a change of the oxidation state of  $Cu_{Zn}$  acceptors through the formation of complexes involving  $Cu_{Zn}$  and  $V_{Zn}$  defects. Additionally, a redshifted secondary line constantly separated by  $\approx 30$  meV from  $[Cu_{Zn}]^{e(-1/-2)}$ -related transitions occurs, for which its origin is still unclear. West et al. suggested the appearance of a second series of radiative transitions separated by  $\approx 225$   $cm^{-1}$  ( $\approx 28$  meV) involving the spin–orbit splitting in the ground state of  $Cu^{2+}$ .<sup>[62]</sup> This hypothesis could strongly be correlated with the spin splitting of the valence (conduction) band maximum (minimum) owing the strong (weak) spin–orbit coupling between the Cu *d*-orbital and O *p*-orbital (Zn *s*-orbital).<sup>[63,64]</sup> Moreover, Dingle et al. reported two  $Cu^{2+}$ -related peaks separated by 0.11 meV at the energy of  $\approx 2.8590$  eV, whose two emission lines were assigned to an identical electronic process taking place at similar but separate sites involving  $^{63}Cu$  and  $^{65}Cu$  isotopes.<sup>[57]</sup> In the present work, the discussed two peaks are largely separated by 0.11 meV. It is worth mentioning that a transition between the  $(Cu^+, h)$  excited state and the  $Cu^{2+}$  ( $E_2$ ) ground state, located at 1 eV below the conduction band minimum, could occur as well under polarized light excitation.<sup>[59]</sup> However, the cathodoluminescence spectra were recorded under unpolarized electron beam. The 5 K cathodoluminescence spectra eventually reveal unambiguously the optical signature and hence the incorporation process of Cu dopants into ZnO NWs as the  $[Cu]/[Zn]_{bath}$  ratio is above 0%.

### 2.4. XANES and XLD Spectra of As-Grown and Thermally Annealed Cu-Doped ZnO Nanowires

To investigate in more detail the local environment around Cu and Zn atoms in Cu-doped ZnO NWs before and after thermal annealing, XANES and XLD spectra were recorded at the ESRF ID12 beamline. The experimental Zn K-edge XANES spectra,



recorded with the polar  $c$ -axis oriented perpendicular (E $\perp$ c) and parallel (E// $c$ ) to the electric field of the linearly polarized X-Ray beam, along with their difference as the XLD spectrum, of Cu-doped ZnO NWs with a [Cu]/[Zn]<sub>bath</sub> ratio of 5%, are shown in **Figure 4a,b**, respectively. The XANES and XLD spectral shape depicts the typical Zn atoms with an oxidation state of 2+ structured in a wurtzite configuration, that is, Zn<sup>2+</sup> cations surrounded by O<sup>2-</sup> anions in a tetrahedral coordination.<sup>[65,66]</sup> It should be mentioned that the spectral shape along with the intensity (amplitude of 1.15) of the Zn K-edge XLD spectra of Cu-doped ZnO NWs was found to be similar regardless of the [Cu]/[Zn]<sub>bath</sub> ratio. These XLD spectra are comparable to those of both high-quality Co-doped ZnO films and Ga-doped ZnO

NWs.<sup>[67,68]</sup> This indicates that 1) the Cu-doped ZnO NWs exhibit a high degree of vertical alignment along the  $c$ -axis (no XLD signal was detected in the substrate plane, i.e., absence of ZnO NWs parallel to the substrate) and that 2) the incorporation process of Cu dopants does not disturb the local wurtzite crystalline quality of ZnO NWs, which is consistent with the Raman scattering spectra and XRD patterns. It is worth noticing that the atomic ratio between the Cu and Zn atoms into the ZnO NWs (denoted as [Cu]/[Zn]<sub>NW</sub>) can be quantitatively determined by comparing directly the edge jump intensity at the Cu K-edge and Zn K-edge. For instance, in the case of Cu-doped ZnO NWs grown with a [Cu]/[Zn]<sub>bath</sub> ratio of 5%, an atomic [Cu]/[Zn]<sub>NW</sub> ratio as low as  $\approx 0.01\%$  was found. Despite the sizeable concentration of

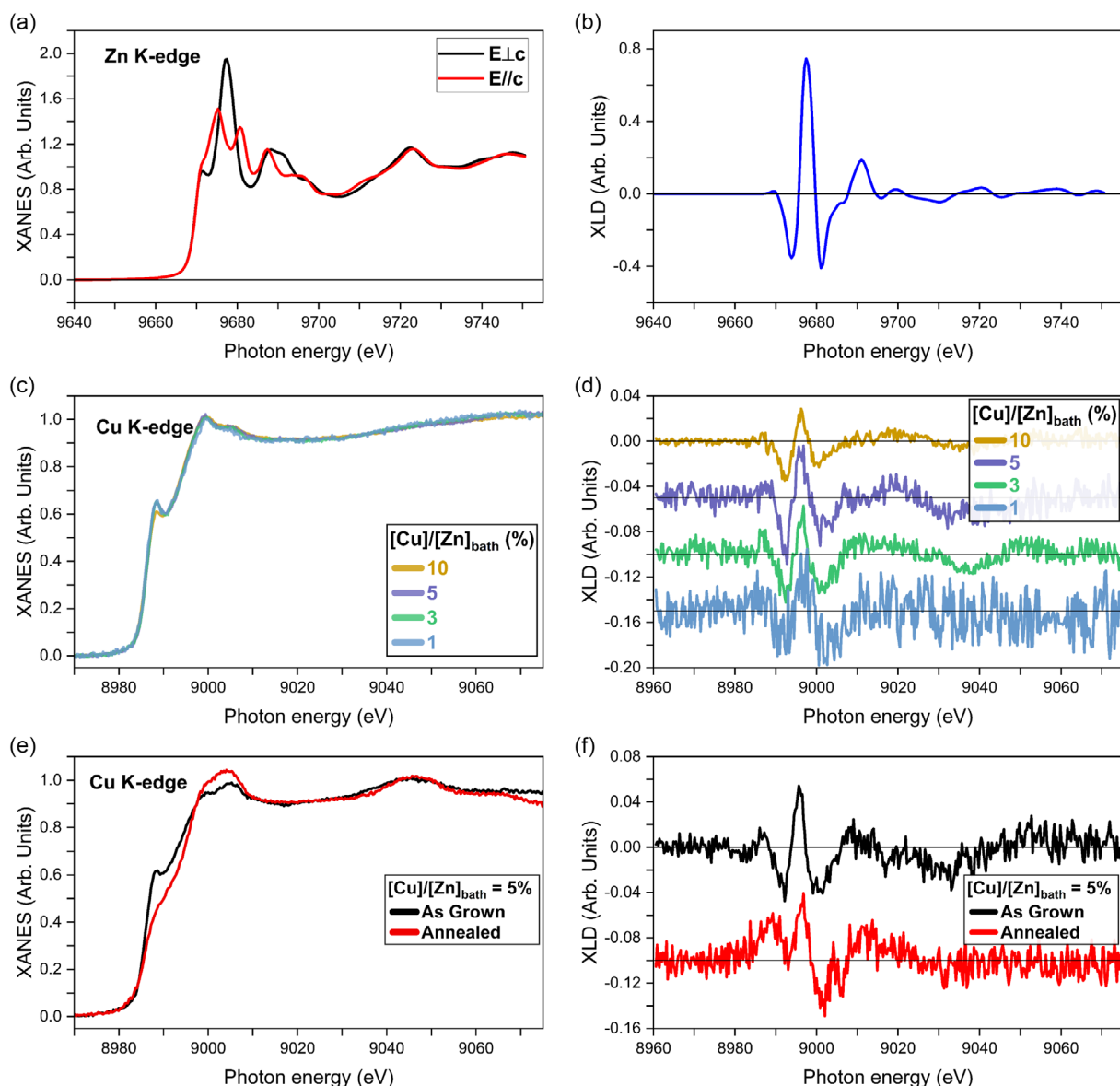


**Figure 4.** Zn K-edge a) XANES and corresponding b) XLD spectra of Cu-doped ZnO NWs grown by CBD with a [Cu]/[Zn]<sub>bath</sub> ratio of 5%. Normalized c) XANES and corresponding d) XLD spectra of ZnO NWs grown by CBD with [Cu]/[Zn]<sub>bath</sub> ratios of 1, 3, 5, and 10% recorded at the Cu K-edge. Normalized e) XANES and corresponding f) XLD spectra of ZnO NWs grown by CBD with a [Cu]/[Zn]<sub>bath</sub> ratio of 5%, before and after thermal annealing at 500 °C for 1 h under O<sub>2</sub> atmosphere.

Cu dopants present in the chemical bath, only a very small amount of Cu dopant is incorporated into the ZnO NWs during the CBD process. This agrees with ICP-MS measurements, where a low atomic  $[Cu]/[Zn]_{NW}$  ratio in the ZnO NWs increasing from 2 ( $\approx 0.0002\%$ ) to 80 ( $\approx 0.008\%$ )  $\mu\text{mol mol}^{-1}$  is achieved through the increase in the  $[Cu]/[Zn]_{bath}$  ratio from 0 to 10%. The normalized isotropic Cu K-edge XANES and corresponding XLD spectra of ZnO NWs grown at different  $[Cu]/[Zn]_{bath}$  ratios are presented in Figure 4c,d, respectively. The isotropic XANES spectra show a similar spectral shape regardless of the  $[Cu]/[Zn]_{bath}$  ratio, exhibiting a peak at the leading edge followed by a prominent one located  $\approx 11$  eV above. In addition, no pre-edge peak occurs within the noise level in the recorded XANES spectra. Interestingly, the present isotropic XANES spectra at the Cu K-edge of Cu-doped ZnO NWs resemble the XANES spectrum recorded for 20% Cu-doped ZnO films grown by reactive magnetron sputtering under optimum growth conditions,<sup>[69]</sup> but significantly differ from the XANES spectrum measured on low-concentrated Cu-doped ZnO polycrystalline pellets.<sup>[70,71]</sup> It should be noted that the XLD spectra at the Cu K-edge are found to exhibit a similar spectral shape that those at the Zn K-edge, which is nearly independent upon the  $[Cu]/[Zn]_{bath}$  ratio. This strongly suggests that few Cu atoms are arranged in a wurtzite structure by substituting for Zn sites as  $\text{Cu}_{Zn}$ . For instance, in the case of Cu-doped ZnO NWs grown with a  $[Cu]/[Zn]_{bath}$  ratio of 5%, a maximum amplitude of  $\approx 0.09$  is reached for the XLD signal at the Cu K-edge, which is much lower than the XLD signal recorded at the Zn K-edge (amplitude of 1.15). As a comparison, an amplitude of about 0.5 of the XLD spectrum at the Cu K-edge is expected when substituting one  $\text{Zn}^{2+}$  ion by one  $\text{Cu}^{2+}$  ion in a ZnO supercell using the bulk lattice constants, according to Finite Difference Method Near Edge Structure (FDMNES) simulations.<sup>[69]</sup> Hence, by comparing the XLD intensities measured at the Cu K-edge and Zn K-edge of ZnO NWs grown with a  $[Cu]/[Zn]_{bath}$  ratio of 5%, only  $15 \pm 5\%$  of the total amount of Cu dopants into ZnO NWs is incorporated as  $\text{Cu}_{Zn}$ . By considering  $4.2 \times 10^{22}$  at  $\text{cm}^{-3}$  of Zn in one ZnO hexagonal crystallographic cell, the  $\text{Cu}_{Zn}$  amount here can thus be calculated by multiplying the intensity ratio of XANES and XLD spectra recorded at the Cu K-edge and Zn K-edge, that is,  $(0.01\%) \times (15\%) \times (4.2 \times 10^{22}$  at  $\text{cm}^{-3}) = 6.3 \times 10^{17}$  at  $\text{cm}^{-3}$  of  $\text{Cu}_{Zn}$ . Following the present approach, the amount of  $\text{Cu}_{Zn}$  acceptor defects in ZnO NWs grown with  $[Cu]/[Zn]_{bath}$  ratios of 1, 3, and 10% is expected to be 1.3, 3.8, and  $12.7 \times 10^{17}$  at  $\text{cm}^{-3}$ , respectively. The majority amount of Cu ( $\approx 85\%$ ) in ZnO NWs grown with a  $[Cu]/[Zn]_{bath}$  ratio of 5% is likely in a  $\text{Cu}_2\text{O}$ -like environment when comparing its isotropic XANES spectrum with that of Cu reference samples.<sup>[69]</sup> Vachhani et al. reported a similar conclusion in the case of Cu-doped ZnO films prepared by pulsed laser deposition, in which most of the Cu atoms are not incorporated into the wurtzite structure, but exhibit a  $\text{CuO}$ -like coordination.<sup>[72]</sup> Before thermal annealing, it is likely that the minority  $\text{Cu}_{Zn}$  dopants are incorporated into the bulk of ZnO NWs, while the majority amount of Cu is located on their surfaces, as suggested in Ref. [15]. After thermal annealing of Cu-doped ZnO NWs grown with a  $[Cu]/[Zn]_{bath}$  ratio of 5% at 500 °C for 1 h under  $\text{O}_2$  atmosphere, a noteworthy change of the isotropic XANES and XLD spectra recorded at Cu K-edge occurs, as depicted in Figure 4e,f, respectively. The isotropic XANES spectra exhibit

the disappearance of the sharp peak at the leading edge along with the widening of the following prominent peak. The XLD spectra further reveal as well the occurrence of a moderate peak around 9890 eV and a slight shift ( $\approx 2$  eV) to higher energies of the highest peak at  $\approx 9000$  eV. The modifications of the XANES and XLD spectra observed in the case of thermally annealed Cu-doped ZnO NWs suggest a change of the electronic structure of the Cu dopants due to a more oxidizing local environment. This indicates again the formation of  $\text{V}_{Zn}$  defects in the vicinity of Cu dopants after thermal annealing, possibly forming  $\text{Cu}_{Zn}$ -related defect complexes as in the cases of Ga-doped ZnO NWs and Sb-doped ZnO NWs.<sup>[14,67,73–75]</sup>

## 2.5. Electrical Properties of As-Grown and Thermally Annealed Cu-Doped ZnO Nanowires

The electrical properties of as-grown and thermally annealed ZnO NWs with a  $[Cu]/[Zn]_{bath}$  ratio varying in the range of 0–10% are studied using two-point probe resistivity measurements on single-object-based bottom transistors, for which the whole process flow of fabrication is schematized in Figure 5a. A fragment of the substrate on which the ZnO NWs were grown was immersed in isopropyl alcohol solution during a sonication process under ultrasound (1), allowing the NWs to be separated from the substrate. The isopropyl alcohol solution containing the dispersed ZnO NWs was subsequently put by drop casting on p++ Si (100) substrates coated with a  $\text{Si}_3\text{N}_4$  insulating layer (2). The present substrate was placed on a heated plate to evaporate the isopropyl alcohol, leaving solely the ZnO NWs in contact with the  $\text{Si}_3\text{N}_4$  insulating layer (3). A single and random ZnO NW was then selected to contact its edges with two metallic electrodes separated by  $\approx 4 \mu\text{m}$  through an optical lithography process. After the development of the photoresist, the contacts acting as the two metallic electrodes consisting of the stack of the 100 nm-thick Ti layer and 250 nm Au layer were achieved by vacuum evaporation followed by a lift-off process, resulting in an operating bottom transistor (4). The electrical characterizations of single-ZnO NWs were performed in ambient atmosphere by measuring the current  $I$  when sweeping an applied voltage  $V$  from  $-1$  to  $+1$  V with a step of 0.1 V between the two electrodes of the device. Therefore, the resistance  $R$  of each ZnO NW was determined as the slope of its corresponding linear  $I$ - $V$  curve, according to the Ohm's law, as shown in Figure S4, Supporting Information. It should be noted that the establishment of a contact resistance can occur during the two-point probe measurements, potentially leading to overestimated electrical resistance values. Therefore, the statistical analysis of the  $R/l$  values of each ZnO NW, where  $l$  is the distance between the two metallic electrodes, was performed as a function of their radius  $r$ , as presented in Figure 5b. The  $R$ ,  $l$ , and  $r$  values for each measured ZnO NW are summarized in Figure S4, Supporting Information. These  $R/l$  values are compared with experimental data from four-point probe measurements on ZnO NWs synthesized by different deposition techniques<sup>[9,11]</sup> and from two-point probe measurements on ZnO NWs grown by CBD.<sup>[15]</sup> It is worth mentioning that, given the radius of ZnO NWs larger than 25 nm, surface effects leading to higher  $R/l$  values from the chemisorption of  $\text{O}_2^-$  and  $\text{OH}^-$  ions can be neglected.<sup>[11,76–78]</sup>

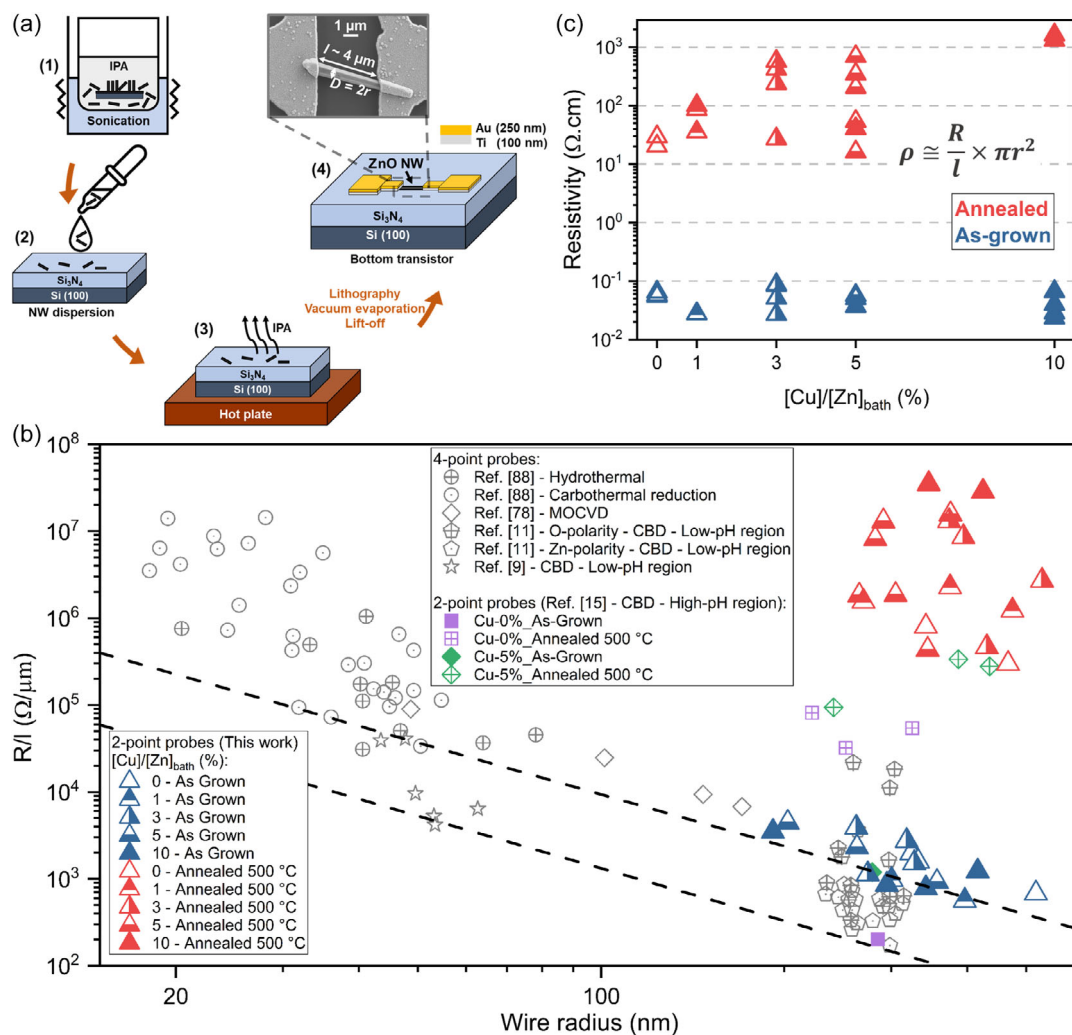


**Figure 5.** a) Fabrication steps of a single-NW-based channel bottom transistor device with its top-view FESEM image. b)  $R/l$  values versus  $r$  of ZnO NWs for the present work assessed by the two-point probe method, along with those reported on ZnO NWs grown by hydrothermal process,<sup>[88]</sup> carbothermal reduction,<sup>[88]</sup> metal-organic chemical vapour deposition,<sup>[78]</sup> and CBD in the low-<sup>[9,11]</sup> and high-pH<sup>[15]</sup> environments. c) Electrical resistivity assessed by two-point probe measurements of ZnO NWs grown by CBD with  $[Cu]/[Zn]_{\text{bath}}$  ratios of 0, 1, 3, 5, and 10%, before and after thermal annealing at 500 °C for 1 h under  $O_2$  atmosphere. The  $R/l$  and resistivity axes are plotted using logarithmic scales.

The dashed lines in Figure 5b, representing isoresistivity values of 4.1 and 28.4 mΩ cm (i.e., typical range of resistivity for Zn-polar ZnO NWs), delimit the bulk-like electrical conduction region where surface effects are negligible, and free electrons are expected to flow across the entire core of the ZnO NWs resulting in  $R/l$  values proportional to  $1/r^2$ .<sup>[9]</sup> The higher  $R/l$  values observed in as-grown ZnO NWs with a radius similar to those of Refs. [11,15] may suggest an apparent overestimation due to the contact resistance. However, the addition of ammonia to the chemical bath is known to lead to oxygen-rich conditions, which promote the formation of  $V_{Zn}$  defects potentially dissociating  $V_{Zn}-3H$  defect complexes acting as shallow donors into low-coordinated  $V_{Zn}-2H$  and  $V_{Zn}-H$  defect complexes leading to increased electrical resistance values.<sup>[44,73]</sup> Therefore, the increase in the initial pH of the chemical bath also accounts

for the higher  $R/l$  values compared to the previous work on ZnO NWs grown by CBD with  $[Cu]/[Zn]_{\text{bath}}$  ratios of 0% and 5% at an initial pH of 10.6 ( $[NH_3]_{\text{bath}} = 600 \text{ mmol L}^{-1}$ ). However, as the ZnO NWs only differ in the  $[Cu]/[Zn]_{\text{bath}}$  ratio used, it is assumed that the effects of the pH of the chemical bath and the effects of the contact resistance remain identical, and thus any differences in the electrical behavior among these unintentionally  $n$ - and Cu-doped ZnO NWs can be attributed to the variation of their electrical properties. Then, the electrical resistivity  $\rho$  was later estimated according to the following equation:  $\rho \cong RS/l$ , where  $S$  refers to the effective electrical conduction section of the ZnO NW, that is,  $S = \pi r^2$ , considering the bulk-like electrical conduction in a flat-band regime.<sup>[78]</sup> The resulting  $\rho$  values of as-grown and thermally annealed ZnO NWs with a  $[Cu]/[Zn]_{\text{bath}}$  ratio varying in the range of 0–10% are shown

in Figure 5c. The as-grown ZnO NWs present low  $\rho$  values lying in the range of 0.042–0.087  $\Omega$  cm, regardless of the  $[\text{Cu}]/[\text{Zn}]_{\text{bath}}$  ratio. In contrast, the thermally annealed ZnO NWs exhibit higher mean values of  $\rho$  progressively increasing from 12.9 to 1479.4  $\Omega$  cm as the  $[\text{Cu}]/[\text{Zn}]_{\text{bath}}$  ratio is increased from 0 to 10%. The compensatory process with Cu dopants in as-grown ZnO NWs regardless of the  $[\text{Cu}]/[\text{Zn}]_{\text{bath}}$  ratio is thus fairly poor. Concerning the thermally annealed ZnO NWs, their higher electrical resistivity values, regardless of the  $[\text{Cu}]/[\text{Zn}]_{\text{bath}}$  ratio, is understandable beyond the influence of a contact resistance as the sign of an efficient compensatory process involving Cu dopants after thermal annealing. The electrical resistivity involving the intrinsic semiconducting properties can be defined as  $\rho = \frac{1}{nq\mu}$ , where  $n$ ,  $q$ , and  $\mu$  refers to the density of free electrons ( $\text{cm}^{-3}$ ), the absolute value of the electron charge ( $1.6 \times 10^{-19}$  C), and the mobility of free electrons ( $\text{cm}^2\text{V}^{-1}\text{s}^{-1}$ ), respectively. If a compensatory process occurs in Cu-doped ZnO NWs, a decrease in the density and mobility of free electrons would be expected as reported in thin Cu-doped ZnO films in Refs. [79,80]. The condition satisfying this hypothesis could thus be expressed as  $n^{\text{ZnO}} \times \mu^{\text{ZnO}} > n^{\text{Cu:ZnO}} \times \mu^{\text{Cu:ZnO}}$ , where  $n^i$  and  $\mu^i$  are the density and mobility of free electrons in unintentionally  $n$ -doped ( $i = \text{ZnO}$ ) and Cu-doped ( $i = \text{Cu:ZnO}$ ) ZnO NWs, respectively. The present condition would unambiguously lead to higher electrical resistivity values of ZnO NWs when doped with Cu dopants (i.e.,  $\rho^{\text{ZnO}} < \rho^{\text{Cu:ZnO}}$ ). In the present work, a progressive increase in the values of  $\rho$  of ZnO NWs is achieved after thermal annealing and as the  $[\text{Cu}]/[\text{Zn}]_{\text{bath}}$  ratio is increased from 0 to 10%. By considering that the reported mobility of free electrons lies in the range of 15–60  $\text{cm}^2\text{V}^{-1}\text{s}^{-1}$  [15,35] in unintentionally  $n$ -doped and intentionally doped ZnO NWs, this is mainly attributed to a progressive decrease in the values of the density of free electrons in ZnO NWs. The evolution of the electrical resistivity involves the engineering of H- and N-related defects in the ZnO NWs, [35] the surface-to-bulk migration process of Cu dopants, and the change of the oxidation state of  $\text{Cu}_{\text{Zn}}$  acceptor defects.

### 3. Discussion

The present work highlights the compensatory doping process at work using the incorporation of different amounts of Cu atoms into ZnO NWs grown by CBD, as illustrated in Figure 6. As the nucleation and growth processes of ZnO NWs by CBD proceed, the unintentional incorporation process of shallow donors as  $\text{H}_{\text{BC}}$ ,  $\text{H}_{\text{O}}$ , and  $\text{V}_{\text{Zn}}-3\text{H}$  defect complexes result in a high density of free electrons lying in the range of  $5.0 \times 10^{17}$ – $3.1 \times 10^{19}\text{ cm}^{-3}$ . [9–11] Moreover, through the addition of ammonia in the chemical bath to tune the pH in the region where electrostatic interactions are favorable for the incorporation process of Cu atoms into ZnO NWs, a significant amount of deep acceptors such as  $\text{V}_{\text{Zn}}-\text{N}_{\text{O}}-\text{H}$  defect complexes is expected to form as well. [35] Therefore, the electrical resistivity of ZnO NWs is conducted by the concentration of these defects and defect complexes acting as shallow donors and deep acceptors. In the scenario where an additional Cu dopant solution is added to the chemical bath for inducing the compensatory doping process and hence reducing the screening effect of the piezoelectric potential for PNGs, [15] the incorporation process of  $\text{Cu}_{\text{Zn}}$  as acceptors into ZnO NWs is thermodynamically favorable owing to its low formation energy. [26] The incorporation process of Cu atoms is assisted by electrostatic forces between the positively charged  $\text{Cu}(\text{NH}_3)_4^{2+}$  complexes and the negatively charged  $c$ -polar top faces of ZnO NWs. Nevertheless, the as-grown Cu-doped ZnO NWs obtained with  $[\text{Cu}]/[\text{Zn}]_{\text{bath}}$  ratios of 1, 3, 5, and 10% exhibit an electrical resistivity in the same order of magnitude as the as-grown unintentionally  $n$ -doped ZnO NWs obtained with a  $[\text{Cu}]/[\text{Zn}]_{\text{bath}}$  ratio of 0%. This unexpected behavior is attributed to a reduction of the concentration of  $\text{V}_{\text{Zn}}-3\text{H}$  defect complexes as the pH of the chemical bath increases, which favors the formation of  $\text{V}_{\text{Zn}}$  defects, [44,73] as well as the additional formation of other Cu-related defects with unknown electronic properties, which should be distinguished from  $\text{Cu}_{\text{Zn}}$ . The latter hypothesis is strongly supported by XLD measurements performed on ZnO NWs grown with a  $[\text{Cu}]/[\text{Zn}]_{\text{bath}}$  ratio

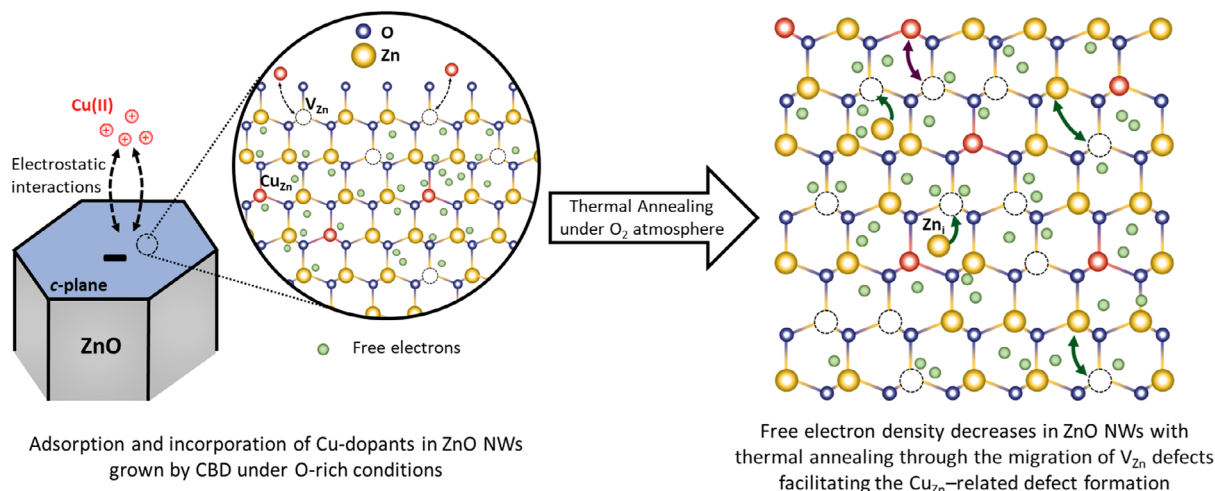


**Figure 6.** Adsorption and incorporation processes of Cu atoms in ZnO NWs grown by CBD in the high-pH environment, along with the migration processes of  $\text{Cu}_{\text{Zn}}$  as acceptors assisted by the massive formation and migration processes of  $\text{V}_{\text{Zn}}$  following thermal annealing under  $\text{O}_2$  atmosphere at 500  $^\circ\text{C}$ .



of 5%, which reveal that only  $(15 \pm 5)\%$  of the total amount of Cu atoms incorporated is found to substitute for Zn sites as  $\text{Cu}_{\text{Zn}}$ . In contrast, the remaining 85% of the total amount of Cu atoms appears to be in a  $\text{Cu}_2\text{O}$ -like environment. Moreover, the significant presence of electrically inactive Cu-related defects located on the surfaces of ZnO NWs is also expected strongly from X-ray photoelectron spectroscopy measurements,<sup>[15]</sup> which does contribute to the compensatory doping process. Given the expected intermediate formation energy of  $\text{V}_{\text{Zn}}\text{-N}_\text{O}\text{-H}$  defect complexes acting as deep acceptors in ZnO NWs grown in a high-pH environment,<sup>[35]</sup> the presence of  $\text{Cu}_{\text{Zn}}$  could further lead to the formation of  $\text{Cu}_{\text{Zn}}\text{-N}_\text{O}\text{-H}$  defect complexes with unknown electronic properties. Before thermal annealing, the incorporation process of Cu atoms into ZnO NWs with a significant concentration varying from  $6.71 \pm 1.11 \times 10^{17}$  to  $3.58 \pm 0.56 \times 10^{18}$  at  $\text{cm}^{-3}$  as shown by ICP-MS measurements is thus not favorable for the compensatory doping process, which is fairly limited.

After thermal annealing at 500 °C for 1 h under  $\text{O}_2$  atmosphere, the notable and progressive increase in the electrical resistivity of Cu-doped ZnO NWs obtained with  $[\text{Cu}]/[\text{Zn}]_{\text{bath}}$  ratios of 1, 3, 5, and 10% mainly originates from the three following phenomena: i) the reduction of the concentration of shallow donors as  $\text{H}_{\text{BC}}$  and  $\text{V}_{\text{Zn}}\text{-3H}$  defect complexes, which are unstable at that high annealing temperature,<sup>[35]</sup> ii) the active formation of  $\text{V}_{\text{Zn}}\text{-N}_\text{O}\text{-H}$  defect complexes as deep acceptors,<sup>[44,81]</sup> and iii) the formation of electrically active Cu-related defects acting as acceptors, all of them leading to a decrease in the density of free electrons and consequently to the higher electrical resistivity. Although the concentration of  $\text{Cu}_{\text{Zn}}$  in Cu-doped ZnO NWs is roughly constant before and after thermal annealing, their local environment becomes more oxidizing, as revealed by XLD and XANES spectra. This indicates that the highest electrical resistivity in thermally annealed Cu-doped ZnO NWs is driven by additional Cu-related defects, as supported by 5 K cathodoluminescence spectroscopy, which shows an enhanced structured green emission band only after thermal annealing. This further suggests strongly the formation of defect complexes involving  $\text{Cu}_{\text{Zn}}$  and  $\text{V}_{\text{Zn}}$  following thermal annealing, which could explain both the increased electrical resistivity and the enhanced structured green emission band in Cu-doped ZnO NWs. Under oxygen-rich conditions, the formation of defect complexes involving P, As, Sb, and Ga dopants with  $\text{V}_{\text{Zn}}$  in ZnO has largely been documented due to their low formation energy and act as deep acceptors, such as  $\text{M}_{\text{Zn}}\text{-}n\text{V}_{\text{Zn}}$  ( $\text{M} = \text{P, As, Sb, Ga; } n = 1, 2, 3$ ),<sup>[14,67,75,82]</sup> or as shallow donors in proximity to H atoms, like  $\text{V}_{\text{Zn}}\text{-Ga}_{\text{Zn}}\text{-3H}$  and  $\text{V}_{\text{Zn}}\text{-Al}_{\text{Zn}}\text{-2H}$ .<sup>[67,83]</sup> The formation of defect complexes involving  $\text{Cu}_{\text{Zn}}$  and  $\text{V}_{\text{Zn}}$  could thus arise from the migration process of  $\text{Cu}_{\text{Zn}}$ , which is promoted by the favorable formation and migration processes of  $\text{V}_{\text{Zn}}$  following thermal annealing under  $\text{O}_2$  atmosphere. It is well known that, under oxygen-rich conditions,  $\text{V}_{\text{Zn}}$  are efficiently formed in ZnO NWs owing to their low formation energy and can further migrate in an isotropic manner by benefiting from the relatively low migration barrier of 1.4 eV.<sup>[73]</sup> As a consequence, following thermal annealing at 500 °C under  $\text{O}_2$  atmosphere,  $\text{V}_{\text{Zn}}$  are strongly mobile, which favor the migration process of  $\text{Cu}_{\text{Zn}}$  and the formation of  $\text{Cu}_{\text{Zn}}$ -related defect complexes. This could account for the changes in the electronic structure of  $\text{Cu}_{\text{Zn}}$ , which can act as highly efficient ( $\text{Cu}_{\text{Zn}}^{2+}$ ) or poorly efficient

( $\text{Cu}_{\text{Zn}}^{1+}$ ) acceptors.<sup>[58]</sup> When combining the formation and migration processes of  $\text{Cu}_{\text{Zn}}$ -related species as described above, a strong reduction in the density of free electrons in ZnO NWs occurs through enhanced electron-hole pair recombination, that is, a compensatory doping process involving  $\text{Cu}_{\text{Zn}}$ -related acceptors and intrinsic/extrinsic donors in ZnO NWs. For instance, negatively ionized  $[\text{Cu}_{\text{Zn}}^{1+}(3\text{d}^{10})]^-$  acceptors may associate with singly positive ionized  $\text{Zn}_i^+(4\text{s}^1)$  donors to form neutral  $\{[\text{Cu}^{2+}(3\text{d}^{10})\text{Zn}_i^+]\}^0$  defect complexes.<sup>[58,62]</sup> The steady increase in the electrical resistivity of thermally annealed Cu-doped ZnO NWs is in excellent agreement with the progressive formation of  $\text{Cu}_{\text{Zn}}$  acceptors as the  $[\text{Cu}]/[\text{Zn}]$  ratio is increased from 1 to 10%, as confirmed by ICP-MS, XANES, and XLD measurements. The present findings reveal the powerful combination of ICP-MS with XANES and XLD measurements to thoroughly investigate the intentional doping of ZnO NWs. They further revisit the compensatory doping process of ZnO NWs with Cu and open alternative pathways in the fields of optoelectronics, piezoelectricity, and photocatalysis to tune the optical and electrical properties of ZnO NWs as a powerful mean for enhancing the performance of the related devices.

#### 4. Conclusion

In summary, the effects of the compensatory doping of ZnO NWs grown by CBD with Cu, along with the thermal annealing at 500 °C under  $\text{O}_2$  atmosphere, have been investigated both qualitatively and quantitatively at the local scale. The Cu(II) species have successfully been adsorbed and incorporated into ZnO NWs as CBD proceeded, exhibiting an increase in the atomic  $[\text{Cu}]/[\text{Zn}]_{\text{NW}}$  ratio from around  $4.5 \times 10^{16}$  to  $3.6 \times 10^{18}$  at  $\text{cm}^{-3}$  as the  $[\text{Cu}]/[\text{Zn}]_{\text{bath}}$  ratio is increased from 0 to 10%. The chemical bath has been maintained in a high-pH environment by adding ammonia, in which oxygen-rich conditions along with attractive electrostatic forces between the positively charged Cu(II) species and the negatively charged polar  $c$ -planes of ZnO NWs occur during the CBD process. The incorporated Cu has not altered the crystalline quality of ZnO NWs, as shown by XRD and Raman scattering. XANES and XLD spectra have confirmed the formation of  $\text{Cu}_{\text{Zn}}$ -related defects in ZnO NWs, with their concentration increasing from 1.3 to  $12.7 \times 10^{17}$   $\text{cm}^{-3}$  as the  $[\text{Cu}]/[\text{Zn}]_{\text{bath}}$  ratio is increased from 1 to 10%. Interestingly, while the concentration of incorporated Cu remains unchanged after thermal annealing, their electronic structure has undergone significant modifications related to a more oxidizing local environment. 5 K cathodoluminescence spectra and two-point probe electrical resistivity measurements have demonstrated the need for thermally activating the  $\text{Cu}_{\text{Zn}}$ -related defect complexes in ZnO NWs. The 5 K cathodoluminescence spectra have shown an enhanced structured green emission band with strong phonon coupling in thermally annealed Cu-doped ZnO NWs, which has been attributed to the contributions from  $\text{Cu}_{\text{Zn}}^{e(-1/-2)}$  defects located at 2.856 eV. In the same way, the two-point probe measurements have revealed a notable increase in the electrical resistivity of thermally annealed Cu-doped ZnO NWs from 12.9 to 1479.4  $\Omega\cdot\text{cm}$  as the  $[\text{Cu}]/[\text{Zn}]_{\text{bath}}$  ratio is increased from 0 to 10%. The significant increase in the electrical resistivity and the enhanced structured green

emission band with a strong phonon coupling, along with the constant concentration but the altered local environment of Cu<sub>Zn</sub>-related defects after thermal annealing in ZnO NWs, suggest the formation of Cu<sub>Zn</sub>-related defect complexes involving nearby V<sub>Zn</sub>. These defect complexes likely arise from the migration process of Cu<sub>Zn</sub>, promoted by the favorable formation and migration processes of V<sub>Zn</sub> as thermal annealing under O<sub>2</sub> atmosphere proceeds. These findings have unraveled the incorporation and compensatory doping processes of Cu into ZnO NWs and their relationship with thermal annealing, highlighting their high potential for piezoelectric devices.

## 5. Experimental Section

**Synthesis and Thermal Annealing of ZnO Nanowires:** The polycrystalline ZnO seed layers were first grown by the sol-gel process on precleaned (100) Si substrates. A solution mixing 375 mmol L<sup>-1</sup> of zinc acetate dehydrate (Zn(CH<sub>3</sub>COO)<sub>2</sub>·2H<sub>2</sub>O, Sigma-Aldrich) and 375 mmol L<sup>-1</sup> of monoethanolamine (MEA, Sigma-Aldrich) in pure ethanol was prepared and stirred for 12 h at 60 °C and then at room temperature. The (100) Si substrates, precleaned in an ultrasonic bath with acetone and isopropyl alcohol, were subsequently dipped into the solution under a controlled atmosphere (<16% hygrometry) and finally annealed at 300 °C for 10 min on a hot plate and at 500 °C for 1 h in a regular oven. Subsequently, ZnO NWs were grown on the polycrystalline ZnO seed layer-coated substrates (ZnO/Si or ZnO/Quartz). The polycrystalline ZnO seed layer-coated substrates were placed face down in sealed reactors containing a 54 mL aqueous solution consisting of zinc nitrate hexahydrate (Zn(NO<sub>3</sub>)<sub>2</sub>·6H<sub>2</sub>O, Sigma Aldrich) and hexamethylenetetramine (HMTA, Sigma Aldrich) with an equimolar concentration ratio of 30 mmol L<sup>-1</sup>. The initial pH of the chemical bath (pH<sub>0</sub>) was fixed at ≈11.0 by adding ≈800 mmol L<sup>-1</sup> of ammonia (NH<sub>3</sub>, Sigma Aldrich). In addition, Cu-dopant solutions with a concentration of 0.3, 0.9, 1.5, and 3 mmol L<sup>-1</sup>, previously prepared by dissolving copper nitrate hemi-pentahydrate (Cu(NO<sub>3</sub>)<sub>2</sub>·2.5H<sub>2</sub>O, Sigma Aldrich) in deionized water were added to the chemical bath in order to fix the [Cu(NO<sub>3</sub>)<sub>2</sub>]/[Zn(NO<sub>3</sub>)<sub>2</sub>] ratio at 1, 3, 5, and 10%, respectively. The growth of ZnO NWs was achieved by keeping the sealed reactors in a regular oven heated at 85 °C for 3 h. Finally, the synthesized ZnO NWs were thermally annealed in a tubular furnace at 500 °C under O<sub>2</sub> atmosphere for 1 h.

**Lab-Scale Characterization Techniques:** The in situ measurements of pH and temperature of the chemical bath were achieved through an InLab Versatile Pro pH electrode from Mettler Toledo. The structural morphology and properties of ZnO NWs were assessed with a FEI Quanta 250 FESEM instrument. The chemical composition was determined with a NexION 1000 PERKIN ELMER ICP-MS instrument. A MEINHARD plus Glass Type C and Glass cyclonic at 2 °C were used as nebulizer and spray chamber, respectively. The He flow rates of nebulization, auxiliary and plasma gas were 1.02 mL min<sup>-1</sup>, 1.2 L min<sup>-1</sup>, and 15 L min<sup>-1</sup>, respectively. The radio frequency power was set to 1450 W. A KED mode was used with 4 mL min<sup>-1</sup> He (7% H<sub>2</sub>) as collision gas. The Si substrates were dipped into a ≈1.0% nitric acid solution [HNO<sub>3</sub>, Carlo Erba] for 12 h to dissolve ZnO NWs. The XRD patterns were recorded with a BRUKER D8 Advance diffractometer using Cu Kα<sub>1</sub> radiation (λ = 0.15406 nm) according to the Bragg-Brentano configuration, in the narrow range from 20° to 100° with an acquisition time of 2.5 s for each 0.015° step. The instrumental shift was corrected by aligning the Si (400) diffraction peak to its theoretical value of 69.132°. The ZnO diffraction peaks were assigned according to the ICDD 00-036-1451 file. The X-Ray pole figures were performed with a 5-circle RIGAKU SmartLab diffractometer implemented with a 0D detector. The acquisition was achieved using a Cu Kα radiation (λ = 0.541862 nm), Cu K<sub>β</sub> filter and 2.5° Sollers slits for the Ω, 2θ, φ, and χ angles. The X-Ray pole figure patterns were recorded on the (002), (112), and (101) diffraction peaks at different φ positions ranging from 0° to 360° with 4° step, along with χ varying from 0° to +90° with 1°

step. The pattern for a given symmetrical positive and negative χ angle in the range of -90° to +90° was achieved by integrating the corresponding φ intensity in the range of 0°-180° and 180°-360°, respectively. The full-width-at-half-maximum (FWHM) of the diffraction peak according the χ position was considered to quantitatively measure the average tilt angle of ZnO NWs. The Raman scattering at room temperature was performed with a RENISHAW InVia Qontor equipment in the backscattering configuration, where a 532 nm excitation line of an Ar<sup>+</sup> laser probed the ZnO NW array from the top with a 100× objective and a power of ≈2.5 mW on the sample surface. The spectral calibration was achieved using the theoretical Si Raman line set to 520.7 cm<sup>-1</sup>. The cathodoluminescence spectroscopy was performed with a FEI Inspect F50 FESEM instrument equipped with a GATAN CF302 liquid helium-cooled stage. An electron beam with a 5 kV acceleration voltage and a small spot size (i.e., less than 10 nm) was used to probe the top of the ZnO NW array in a fast scan mode over an area of 5 × 6 μm<sup>2</sup>. A 550 nm focal length monochromator (HORIBA iHR550) equipped with 600 groves mm<sup>-1</sup> diffraction grating was employed to collect the cathodoluminescence signal with the help of a parabolic mirror. The cathodoluminescence spectra were recorded with a thermoelectric-cooled Si charge coupled device (CCD) detector (Andor Technology Newton CCD DU940-P-BU).

**XANES and XLD Measurements:** The XANES at the Zn K-edge and Cu K-edge were collected in the backscattering geometry using a Si drift detector. All the spectra were taken at the ESRF ID12 beamline and normalized to an edge jump of unity.<sup>[84]</sup> The XLD, defined as the difference between the XANES spectra measured with two orthogonal linear polarizations, was measured by flipping at every energy point the linear polarization of the synchrotron light from the vertical to horizontal directions using a 0.9 mm-thick diamond quarter-wave plate, as described in more detail in Refs. [85,86]. The angle of incidence was set to 10° with respect to the sample surface. All the samples were measured at room temperature.

**Thermodynamic Computations:** Thermodynamic simulations were carried out with Visual MINTEQ software to establish the speciation diagrams of Zn(II) and Cu(II) species along with the theoretical solubility plots of ZnO and CuO at 85 °C for each growth condition (i.e., by varying the NH<sub>3</sub> and Cu-dopant solution concentrations). The two Zn<sup>2+</sup> and Cu<sup>2+</sup> single-metallic cations in the aqueous solution, denoted as M<sup>X+</sup>, were capable to form hydroxide or amine complexes with the two possible ligands (i.e., HO<sup>-</sup> and NH<sub>3</sub>, respectively), denoted as L. Hence, the given general reactions were  $nM^{X+} + iL \leftrightarrow M_nL_i^{n \cdot X+}$ , where M<sub>n</sub>L<sub>i</sub><sup>n·X+</sup> is the complex considered with the coordination number *i*. The related stability constants β<sub>*i*</sub><sup>L</sup> associated with each reaction were calculated as  $\beta_i^L = \frac{[M_nL_i^{n \cdot X+}]}{[M^{X+}]^n \cdot [L]^i}$ , whose constants were taken at 25 °C from National Institute of Standards Technology database and those at 85 °C were deduced from Van't Hoff relation. To calculate the theoretical solubility plots for each growth condition, the Zn- and Cu-related solid oxide and hydroxide phases were considered.

## Supporting Information

Supporting Information is available from the Wiley Online Library or from the author.

## Acknowledgements

This work was partially supported by LabEx MINOS under the contract ANR-10-LABX-55-01 and the French RENATECH network through the PTA technological platforms. M.M. held a doctoral fellowship from LabEx MINOS. V.C. also acknowledges financial support from the French National Research Agency through the project IMINEN (ANR-22-CE09-0032). This research also benefited from some of the characterization equipment of the Grenoble INP-CMTC platform and of IUT 1 Chemical Department platform. The authors further acknowledge the ESRF synchrotron for the provision of beamtime and facilities.

## Conflict of Interest

The authors declare no conflict of interest.

## Author Contributions

**Manuel Manrique:** data curation (equal); formal analysis (equal); investigation (equal); visualization (lead); writing—original draft (lead); writing—review and editing (lead). **Bassem Salem:** data curation (equal); funding acquisition (equal); project administration (equal); resources (equal); supervision (equal); validation (equal); writing—review and editing (equal). **Eirini Sarigiannidou:** data curation (equal); formal analysis (equal); investigation (equal); writing—review and editing (equal). **Hervé Roussel:** data curation (equal); formal analysis (equal); investigation (equal); writing—review and editing (supporting). **Fabrice Wilhelm:** data curation (equal); formal analysis (equal); investigation (equal); writing—review and editing (equal). **Fabrice Donatini:** data curation (equal); formal analysis (equal); investigation (equal); writing—review and editing (equal). **Véronique Jacob:** data curation (equal); formal analysis (equal); investigation (equal); writing—review and editing (supporting). **Gwenaél Le Rhun:** data curation (equal); funding acquisition (equal); project administration (equal); resources (equal); supervision (equal); validation (equal); writing—review and editing (equal). **Vincent Consonni:** conceptualization (lead); data curation (equal); funding acquisition (equal); project administration (equal); resources (equal); supervision (equal); validation (equal); writing—original draft (supporting); writing—review and editing (equal).

## Data Availability Statement

The data that support the findings of this study are available from the corresponding author upon reasonable request.

## Keywords

compensatory doping, synchrotron radiations, ZnO nanowires

Received: October 4, 2024

Revised: November 8, 2024

Published online:

- [1] M. Willander, O. Nur, Q. X. Zhao, L. L. Yang, M. Lorenz, B. Q. Cao, C. Czekalla, G. Zimmermann, M. Grundmann, A. Bakin, A. Behrends, M. Al-Suleiman, A. El-Shaer, A. Che Mofor, B. Postels, A. Waag, N. Boukos, A. Travlos, H. S. Kwack, J. Guinard, D. Le Si Dang, *Nanotechnology* **2009**, *20*, 332001.
- [2] J. Briscoe, S. Dunn, *Nano Energy* **2014**, *14*, 15.
- [3] V. Consonni, J. Briscoe, E. Kärber, X. Li, T. Cossuet, *Nanotechnology* **2019**, *30*, 362001.
- [4] V. Consonni, A. M. Lord, *Nano Energy* **2021**, *83*, 105789.
- [5] Z. L. Wang, *Adv. Funct. Mater.* **2008**, *18*, 3553.
- [6] Ü. Özgür, Y. I. Alivov, C. Liu, A. Teke, M. A. Reshchikov, S. Doğan, V. Avrutin, S.-J. Cho, H. Morkoç, *J. Appl. Phys.* **2005**, *98*, 1.
- [7] L. Schmidt-Mende, J. L. MacManus-Driscoll, *Mater. Today* **2007**, *10*, 40.
- [8] S. Xu, Z. L. Wang, *Nano Res.* **2011**, *4*, 1013.
- [9] J. Villafuerte, F. Donatini, J. Kioseoglou, E. Sarigiannidou, O. Chaix-Pluchery, J. Pernot, V. Consonni, *J. Phys. Chem. C* **2020**, *124*, 16652.
- [10] L. Wang, S. Guillemin, J. M. Chauveau, V. Sallet, F. Jomard, R. Brenier, V. Consonni, G. Brémont, *Phys. Status Solidi* **2016**, *13*, 576.
- [11] T. Cossuet, F. Donatini, A. M. Lord, E. Appert, J. Pernot, V. Consonni, *J. Phys. Chem. C* **2018**, *122*, 22767.
- [12] R. K. Pandey, J. Dutta, S. Brahma, B. Rao, C.-P. Liu, *J. Phys. Mater.* **2021**, *4*, 044011.
- [13] Y. Sun, S. Shen, W. Deng, G. Tian, D. Xiong, H. Zhang, T. Yang, S. Wang, J. Chen, W. Yang, *Nano Energy* **2023**, *105*, 108024.
- [14] J. Villafuerte, X. Zhang, E. Sarigiannidou, F. Donatini, O. Chaix-Pluchery, L. Rapenne, M.-Q. Le, L. Petit, J. Pernot, V. Consonni, *Nano Energy* **2023**, *114*, 108599.
- [15] M. Manrique, V. Consonni, S. Boubenia, H. Roussel, M. Zeghouane, S. Labau, S. Cavalaglio, C. Pudda, V. Jacob, G. Le Rhun, B. Salem, *Energy Technol.* **2024**, *12*, 2301381.
- [16] M. D. McCluskey, S. J. Jokela, *J. Appl. Phys.* **2009**, *106*, 1.
- [17] R. D. Shannon, *Acta Crystallogr. A* **1976**, *32*, 751.
- [18] E. Kaminska, I. Pasternak, P. Boguslawski, A. Jezierski, E. Dynowska, R. Jakiela, E. Przewdziecka, A. Piotrowska, J. Kossut, *AIP Conf. Proc.* **2009**, *1199*, 120.
- [19] J. Joo, B. Y. Chow, M. Prakash, E. S. Boyden, J. M. Jacobson, *Nat. Mater.* **2011**, *10*, 596.
- [20] C. Verrier, E. Appert, O. Chaix-Pluchery, L. Rapenne, Q. Rafhay, A. Kaminski-Cachopo, V. Consonni, *Inorg. Chem.* **2017**, *56*, 13111.
- [21] P. Gaffuri, E. Appert, O. Chaix-Pluchery, L. Rapenne, M. Salaün, V. Consonni, *Inorg. Chem.* **2019**, *58*, 10269.
- [22] C. Lausecker, B. Salem, X. Baillin, O. Chaix-Pluchery, H. Roussel, S. Labau, B. Pelissier, E. Appert, V. Consonni, *Inorg. Chem.* **2021**, *60*, 1612.
- [23] A. Baillard, E. Appert, M. Weber, V. Jacob, H. Roussel, L. Rapenne, O. Chaix-Pluchery, V. Consonni, *J. Phys. Chem. C* **2023**, *127*, 8306.
- [24] R. O. James, T. W. Healy, *J. Colloid Interface Sci.* **1972**, *40*, 65.
- [25] D. W. Fuerstenau, K. Osseo-Asare, *J. Colloid Interface Sci.* **1987**, *118*, 524.
- [26] Y. Yan, M. M. Al-Jassim, S. H. Wei, *Appl. Phys. Lett.* **2006**, *89*, 87.
- [27] S. Guillemin, V. Consonni, E. Appert, E. Puyoo, L. Rapenne, H. Roussel, *J. Phys. Chem. C* **2012**, *116*, 25106.
- [28] R. Parize, J. Garnier, O. Chaix-Pluchery, C. Verrier, E. Appert, V. Consonni, *J. Phys. Chem. C* **2016**, *120*, 5242.
- [29] M. Raja, N. Muthukumarasamy, D. Velauthapillai, R. Balasundaraprabhu, *Superlattices Microstruct.* **2014**, *72*, 102.
- [30] R. Parize, J. D. Garnier, E. Appert, O. Chaix-Pluchery, V. Consonni, *ACS Omega* **2018**, *3*, 12457.
- [31] T. Cossuet, H. Roussel, J. M. Chauveau, O. Chaix-Pluchery, J. L. Thomassin, E. Appert, V. Consonni, *Nanotechnology* **2018**, *29*, 475601.
- [32] M. Valtiner, S. Borodin, G. Grundmeier, *Langmuir* **2008**, *24*, 5350.
- [33] C. Kunze, M. Valtiner, R. Michels, K. Huber, G. Grundmeier, *Phys. Chem. Chem. Phys.* **2011**, *13*, 12959.
- [34] N. H. Nickel, K. Fleischer, *Phys. Rev. Lett.* **2003**, *90*, 4.
- [35] J. Villafuerte, O. Chaix-Pluchery, J. Kioseoglou, F. Donatini, E. Sarigiannidou, J. Pernot, V. Consonni, *Phys. Rev. Mater.* **2021**, *5*, 1.
- [36] X. Li, B. Keyes, S. Asher, S. B. Zhang, S. H. Wei, T. J. Coutts, S. Limpijumnong, C. G. Van De Walle, *Appl. Phys. Lett.* **2005**, *86*, 1.
- [37] S. J. Jokela, M. D. McCluskey, *Phys. Rev. B* **2007**, *76*, 6.
- [38] E. V. Lavrov, J. Weber, F. Börrnert, C. G. Van de Walle, R. Helbig, *Phys. Rev. B* **2002**, *66*, 1.
- [39] F. Herklotz, A. Hupfer, K. M. Johansen, B. G. Svensson, S. G. Koch, E. V. Lavrov, *Phys. Rev. B* **2015**, *92*, 1.
- [40] J. L. Lyons, J. B. Varley, D. Steiauf, A. Janotti, C. G. Van De Walle, *J. Appl. Phys.* **2017**, *122*, 035704.
- [41] E. Lavrov, *Phys. B Condens. Matter* **2003**, *340–342*, 195.
- [42] E. V. Lavrov, F. Börrnert, J. Weber, *Phys. Rev. B* **2005**, *71*, 035205.
- [43] C. Bundesmann, N. Ashkenov, M. Schubert, D. Spemann, T. Butz, E. M. Kaidashev, M. Lorenz, M. Grundmann, *Appl. Phys. Lett.* **2003**, *83*, 1974.

- [44] J. Villafuerte, E. Sarigiannidou, F. Donatini, J. Kioseoglou, O. Chaix-Pluchery, J. Pernot, V. Consonni, *Nanoscale Adv.* **2022**, *4*, 1793.
- [45] P. Sundara Venkatesh, V. Ramakrishnan, K. Jeganathan, *Phys. B Condens. Matter* **2016**, *481*, 204.
- [46] Y. Deng, A. D. Handoko, Y. Du, S. Xi, B. S. Yeo, *ACS Catal.* **2016**, *6*, 2473.
- [47] T. Gruber, G. M. Prinz, C. Kirchner, R. Kling, F. Reuss, W. Limmer, A. Waag, *J. Appl. Phys.* **2004**, *96*, 289.
- [48] F. Decremps, J. Pellicer-Porres, A. M. Saitta, J.-C. Chervin, A. Polian, *Phys. Rev. B* **2002**, *65*, 092101.
- [49] K. Samanta, P. Bhattacharya, R. S. Katiyar, W. Iwamoto, P. G. Pagliuso, C. Rettori, *Phys. Rev. B* **2006**, *73*, 1.
- [50] E. V. Lavrov, F. Herklotz, J. Weber, *Phys. Rev. B* **2009**, *79*, 1.
- [51] R. Heinhold, A. Neiman, J. V. Kennedy, A. Markwitz, R. J. Reeves, M. W. Allen, *Phys. Rev. B* **2017**, *95*, 1.
- [52] B. K. Meyer, H. Alves, D. M. Hofmann, W. Kriegseis, D. Forster, F. Bertram, J. Christen, A. Hoffmann, M. Straßburg, M. Dworzak, U. Haboeck, A. V. Rodina, *Phys. Status Solidi* **2004**, *241*, 231.
- [53] S. Guillemin, V. Consonni, L. Rapenne, E. Sarigiannidou, F. Donatini, G. Bremond, *RSC Adv.* **2016**, *6*, 44987.
- [54] C. Soci, A. Zhang, B. Xiang, S. A. Dayeh, D. P. R. Aplin, J. Park, X. Y. Bao, Y. H. Lo, D. Wang, *Nano Lett.* **2007**, *7*, 1003.
- [55] B. K. Meyer, J. Sann, S. Lautenschläger, M. R. Wagner, A. Hoffmann, *Phys. Rev. B* **2007**, *76*, 184120.
- [56] J. W. Sun, Y. M. Lu, Y. C. Liu, D. Z. Shen, Z. Z. Zhang, B. Yao, B. H. Li, J. Y. Zhang, D. X. Zhao, X. W. Fan, *J. Appl. Phys.* **2007**, *102*, 043522.
- [57] R. Dingle, *Phys. Rev. Lett.* **1969**, *23*, 579.
- [58] H. Qiu, F. Gallino, C. Di Valentin, Y. Wang, *Phys. Rev. Lett.* **2011**, *106*, 1.
- [59] P. Dahan, V. Fleurov, P. Thurian, R. Heitz, A. Hoffmann, I. Broser, *J. Phys. Condens. Matter* **1998**, *10*, 2007.
- [60] M. A. Reshchikov, V. Avrutin, N. Izyumskaya, R. Shimada, H. Morkoç, S. W. Novak, *J. Vac. Sci. Technol. B* **2009**, *27*, 1749.
- [61] X. H. Huang, C. Zhang, C. B. Tay, T. Venkatesan, S. J. Chua, *Appl. Phys. Lett.* **2013**, *102*, 111106.
- [62] C. West, D. J. Robbins, P. J. Dean, W. Hayes, *Phys. B+C* **1983**, *116*, 492.
- [63] M. Ferhat, A. Zaoui, R. Ahuja, *Appl. Phys. Lett.* **2009**, *94*, 1.
- [64] A. Ciechan, P. Bogusławski, *Sci. Rep.* **2021**, *11*, 1.
- [65] A. Ney, K. Ollefs, S. Ye, T. Kammermeier, V. Ney, T. C. Kaspar, S. A. Chambers, F. Wilhelm, A. Rogalev, *Phys. Rev. Lett.* **2008**, *100*, 157201.
- [66] K. M. McPeak, M. A. Becker, N. G. Britton, H. Majidi, B. A. Bunker, J. B. Baxter, *Chem. Mater.* **2010**, *22*, 6162.
- [67] E. Sarigiannidou, P. Gaffuri, F. Wilhelm, J. Kioseoglou, A. Rogalev, E. Nikidis, E. Appert, V. Consonni, *Phys. Rev. Mater.* **2023**, *7*, 076001.
- [68] V. Ney, B. Henne, J. Lumetzberger, F. Wilhelm, K. Ollefs, A. Rogalev, A. Kovacs, M. Kieschnick, A. Ney, *Phys. Rev. B* **2016**, *94*, 1.
- [69] V. Ney, V. Venkataraman, F. Wilhelm, A. Rogalev, A. Ney, *J. Appl. Phys.* **2019**, *126*, 143904.
- [70] P. S. Vachhani, G. Dalba, R. K. Ramamoorthy, F. Rocca, O. Šipr, A. K. Bhatnagar, *J. Phys. Condens. Matter* **2012**, *24*, 506001.
- [71] O. Šipr, J. Vackáľ, P. S. Vachhani, R. K. Ramamoorthy, G. Dalba, A. K. Bhatnagar, F. Rocca, *J. Phys. Conf. Ser.* **2013**, *430*, 012128.
- [72] P. S. Vachhani, O. Šipr, A. K. Bhatnagar, R. K. Ramamoorthy, R. J. Choudhary, D. M. Phase, G. Dalba, A. Kuzmin, F. Rocca, *J. Alloys Compd.* **2016**, *678*, 304.
- [73] A. Janotti, C. G. Van de Walle, *Phys. Rev. B* **2007**, *76*, 165202.
- [74] D. O. Demchenko, B. Earles, H. Y. Liu, V. Avrutin, N. Izyumskaya, Ü. Özgür, H. Morkoç, *Phys. Rev. B* **2011**, *84*, 1.
- [75] S. Limpijumngong, S. B. Zhang, S. H. Wei, C. H. Park, *Phys. Rev. Lett.* **2004**, *92*, 1.
- [76] A. Soudi, C. H. Hsu, Y. Gu, *Nano Lett.* **2012**, *12*, 5111.
- [77] A. M. Lord, T. G. Maffei, M. W. Allen, D. Morgan, P. R. Davies, D. R. Jones, J. E. Evans, N. A. Smith, S. P. Wilks, *Appl. Surf. Sci.* **2014**, *320*, 664.
- [78] A. De Luna Bugallo, F. Donatini, C. Sartel, V. Sallet, J. Pernot, *Appl. Phys. Express* **2015**, *8*, 025001.
- [79] H. L. Pan, B. Yao, T. Yang, Y. Xu, B. Y. Zhang, W. W. Liu, D. Z. Shen, *Appl. Phys. Lett.* **2010**, *97*, 2.
- [80] M. Suja, S. B. Bashar, M. M. Morshed, J. Liu, *ACS Appl. Mater. Interfaces* **2015**, *7*, 8894.
- [81] C. Opoku, A. S. Dahiya, F. Cayrel, G. Poulin-Vittrant, D. Alquier, N. Camara, *RSC Adv.* **2015**, *5*, 69925.
- [82] B. Puchala, D. Morgan, *Phys. Rev. B* **2012**, *85*, 1.
- [83] Y. K. Frodason, K. M. Johansen, T. S. Bjørheim, B. G. Svensson, A. Alkauskas, *Phys. Rev. B* **2018**, *97*, 104109.
- [84] A. Rogalev, F. Wilhelm, *Phys. Met. Metallogr.* **2015**, *116*, 1285.
- [85] A. Rogalev, J. Goulon, C. Goulon-Ginet, C. Malgrange, in *Magnetism and Synchrotron Radiation* (Eds.: E. Beaurepaire, J. P. Kappler, G. Krill, F. Scheurer), Springer, Berlin, Heidelberg, **2001**, pp. 60–86.
- [86] A. Rogalev, F. Wilhelm, J. Goulon, G. Goujon, in *Magnetism and Synchrotron Radiation: Towards the Fourth Generation Light Sources*, Springer, Cham **2013**, Vol. 151, pp. 289–314.
- [87] A. Degen, M. Kosec, *J. Eur. Ceram. Soc.* **2000**, *20*, 667.
- [88] A. M. Lord, T. G. Maffei, A. S. Walton, D. M. Kepaptsoglou, Q. M. Ramasse, M. B. Ward, J. Köble, S. P. Wilks, *Nanotechnology* **2013**, *24*, 435706.